

1 Hydrodynamic and biochemical impacts on the development of 2 hypoxia in the Louisiana–Texas shelf Part 1: roles of nutrient 3 limitation and plankton community

4 Yanda Ou¹ and Z. George Xue^{1,2,3}

5 ¹Department of Oceanography and Coastal Sciences, Louisiana State University, Baton Rouge, LA, 70803, USA.

6 ²Center for Computation and Technology, Louisiana State University, Baton Rouge, LA, 70803, USA.

7 ³Coastal Studies Institute, Louisiana State University, Baton Rouge, LA, 70803, USA

8 *Correspondence to:* Z. George Xue (zxue@lsu.edu)

9 **Abstract.** A three-dimensional coupled hydrodynamic–biogeochemical model with multiple nutrient and plankton functional
10 groups was developed and adapted to the Gulf of Mexico to investigate the role of nutrients and the complexity of plankton
11 community in dissolved oxygen (DO) dynamics. A 15-year hindcast was achieved covering the period of 2006–2020.
12 Extensive model validation against *in situ* data demonstrates that the model was capable of reproducing vertical distributions
13 of DO, spatial distributions of bottom DO concentration, as well as their interannual variations. Model results indicated that
14 while nitrogen (N) limitation was more commonly found in the shallow (< 20 m) middle and west shelf, phosphorus (P) and
15 silicon (Si) limitations could be more spreading on the shelf than previously reported. The seasonality of primary and secondary
16 production exhibited a bi-peak (in late spring and early summer) pattern, which was contributed by both nanophytoplankton
17 and the dominated diatom groups. DO consumption at the sediment layers was mostly contributed by zooplankton mortality
18 and egestion processes. The plankton community in the water column in general, produced more DO than it consumed. In
19 waters within 2 m above the bottom, there was a higher chance that DO consumption could exceed production. Nutrient
20 limitation, interactions (competition, grazing, and predation behaviors) among plankton groups, and shifts in net DO
21 contribution from the community (i.e., (photosynthesis - total respiration)/total biomass) complicated hypoxia development
22 under different nutrient reduction strategies. Sensitivity tests indicate that a triple riverine nutrient reduction (N, P, and Si) of
23 60 % is needed to reach the goal of a 5000 km² hypoxic zone.

24

25 1 Introduction

26 The Louisiana–Texas (LaTex) shelf in the northern Gulf of Mexico (nGoM) has one of the most notorious recurring hypoxia
27 in the world (bottom dissolved oxygen (DO) < 2 mg L⁻¹, Rabalais et al., 2002; Rabalais et al., 2007a; Justić and Wang, 2014).
28 Regular mid-summer cruises since 1985 show that hypoxia usually first emerges in mid-May and persists through mid-
29 September. The hypoxic zone can cover as big as 23,000 km² and has a volume of up to 140 km³ (Rabalais and Turner, 2019;

30 Rabalais and Baustian, 2020). Although N is the ultimate limiting nutrient, P load reduction would also lead to a significant
31 reduction of the hypoxia area (Fennel and Laurent, 2018). Transient P limitation on the shelf (Laurent et al., 2012; Sylvan et
32 al., 2007) was deemed to be associated with the delayed onset and reduction of the hypoxia area. Sensitivity experiments of
33 hypoxia area reduction to different nutrient reduction strategies by Fennel and Laurent (2018) suggested that to meet the
34 hypoxic area reduction goal ($< 5,000 \text{ km}^2$ in a 5-year running average) set by the Hypoxia Task Force (2008), a dual nutrient
35 strategy with a reduction of 48 % of total nitrogen (N) and inorganic phosphorus (P) would be the most effective way.

36

37 Coastal eutrophication in the LaTex shelf leads to a high rate of microbial respiration and depletion of DO (Rabalais et al.,
38 2007b). Incubation studies in the LaTex shelf suggested that sediment oxygen consumption (SOC) accounted for 20 ± 4 %
39 (Murrell and Lehrter, 2011) to 25 ± 5.3 % (McCarthy et al., 2013) of below-pycnocline respiration, nearly 7-fold greater than
40 the corresponding percentage in waters overlying sediments (3.7 ± 0.8 %, about 20 cm above sediments in McCarthy et al.,
41 2013). Incubation experiments indicated the SOC over the total respiration rate at sediments and overlying water was ~ 87 %
42 (McCarthy et al., 2013). The numerical study by Fennel et al. (2013) calculated the corresponding SOC fraction which reached
43 60 % when applying the water respiration rates of Murrell and Lehrter (2011) and sediment respiration rates of Rowe et al.
44 (2002). Another numerical study (Yu et al., 2015) also pointed out that in the LaTex shelf, oxygen consumption at the bottom
45 water layer was more associated with SOC rather than water column respiration. According to in-situ data and statistical
46 analysis, SOC could be estimated using the bottom temperature and DO concentration (e.g., Hetland and DiMarco, 2008).
47 Nevertheless, many numerical studies treated SOC only associated with the abundance of organic matter in the sediment (e.g.,
48 Justić and Wang, 2014; Fennel et al., 2006; 2011). For example, an instantaneous remineralization parameterization used by
49 Fennel et al. (2006, 2011) estimated SOC as a function of sediment detritus and phytoplankton. Using this scheme, Große et
50 al. (2019) found that the simulated SOC was supported by Mississippi N supply (51 ± 9 %), Atchafalaya N supply (33 ± 9 %),
51 and open-boundary N supply (16 ± 2 %). However, the instantaneous parameterization tends to underestimate SOC at the peak
52 of blooms yet overestimate SOC after the blooms. In a realistic environment, there should be a lag between the blooms and
53 the peak SOC (Fennel et al., 2013). Recently, developments of coupled sediment–water models emphasized the importance of
54 biogeochemical processes in sediments on the SOC dynamics and evolution of bottom hypoxia in the shelf (Moriarty et al.,
55 2018; Laurent et al., 2016). However, coupled sediment–water models are computationally more expensive than a simplified
56 parameterization of SOC. Especially for long-term simulations and time-sensitive forecasts, it is crucial to balance the model's
57 efficiency with its complexity.

58

59 In addition to SOC and excess nutrient supply from the rivers, water column stratification also plays an important role in
60 regulating the variability of bottom DO concentration in the LaTex shelf. Strong stratification prohibits ventilation of DO and
61 thus results in reduced DO supply to the bottom water layer (Hetland and DiMarco, 2008; Bianchi et al., 2010; Fennel et al.,
62 2011, 2013, 2016; Justić and Wang, 2014; Wang and Justić, 2009; Feng et al., 2014; Yu et al., 2015; Laurent et al., 2018). On
63 the shelf, the Mississippi and the Atchafalaya plume introduces buoyancy, leading to a stable water column and weak DO

64 ventilation processes (Mattern et al., 2013; Fennel and Testa, 2019). Due to the different distances from major river mouths,
65 the influence of freshwater-induced buoyancy would vary along the shelf. Moreover, the transports and deposition processes
66 of organic matter are affected by the coastal along-shore current systems resulting in a SOC gradient across the shelf. For
67 instance, Hetland and DiMarco (2008) pointed out that in the west of Terrebonne Bay, where stratification is usually weak,
68 bottom hypoxia is mainly controlled by bottom respiration.

69
70 The phytoplankton blooms on the shelf result from both cyanobacteria and diatoms (Wawrik and Paul, 2004; Schaeffer et al.,
71 2012; Chakraborty et al., 2017). In the Mississippi River plume, diatoms were found as the most diverse algal class accounting
72 for over 42 % of all unique genotypes observed (Wawrik and Paul, 2004). Cruises data in the nGoM indicated that diatoms
73 accounted for ~50 to ~65 % (inner-shelf) and ~33 to ~64 % (mid-shelf) of chlorophyll *a* in winter and spring, and ~30 % to
74 ~46 % (inner-shelf) during summer and fall, respectively (Chakraborty and Lohrenz, 2015). A field survey documented that
75 the biovolume contribution of diatoms to the total phytoplankton could be as high as 80 % and 70 % during the upwelling
76 seasons in 2013 and 2014, respectively (Anglès et al., 2019). While a lot of existing studies indicated N and P were more
77 limited than Si on the shelf (e.g., for cruises in 2004 in Quigg et al., 2011; for cruises in 2012 in Zhao and Quigg, 2014; for
78 cruises in 1984, 1994, 2005, 2010, and 2011 in Turner and Rabalais, 2013), Si limitation has also been reported for both plume
79 and shelf water. Based on cruises studies in the plume of the Mississippi River in 1992 and 1993, strong Si limitation in spring
80 was found due to the increasing N:Si ratio in the Mississippi River water (Nelson and Dortch, 1996). Cruise measurements in
81 1987 and 1988 also suggested the likelihood of Si limitation, which sometimes overwhelmed the N limitation (Dortch and
82 Whitley, 1992).

83
84 Numerical studies for hypoxia in the LaTex shelf were developed mostly based on observations that emphasized N and P as
85 limiting nutrients (e.g., Hetland and DiMarco, 2008; Fennel et al., 2006, 2011, 2013; Laurent et al., 2012; Laurent and Fennel,
86 2014; Fennel and Laurent, 2018; Justić et al., 2003; Justić et al., 2007; Justić and Wang, 2014; Große et al., 2019; Moriarty et
87 al., 2018). In addition, most existing models utilized an over-simplified lower trophic level model (one phytoplankton + one
88 zooplankton function group or only one phytoplankton group). The recycling of nutrients in water columns and the associated
89 biogeochemical processes, which may be important to hypoxia evolution (e.g., in the Chesapeake Bay by Testa and Kemp,
90 2012), could be over-simplified. In this study, we aimed to 1) investigate the cycling of silicate and its contribution to the
91 hypoxia evolution in the LaTex shelf; and 2) assess the impacts of the complexity of the plankton community on DO dynamics.
92 We adapted and modified a coupled physical-biogeochemical model covering the entire Gulf of Mexico (GoM) by introducing
93 the oxygen and P cycles to the North Pacific Ecosystem Model for Understanding Regional Oceanography (NEMURO, Kishi
94 et al. 2007). The model has two phytoplankton and three zooplankton functional groups for a more comprehensive
95 representation of the plankton community. We also modified the instantaneous remineralization parameterization by adding a
96 conceptual sedimentary organic pool (represented by a sedimentary particulate organic N pool, PON_{sed}; Fig. 1) to allow the
97 accumulation of organic matter in the sediment. The sedimentary organic matter pool in our study is supported by a complex

98 plankton community, including two phytoplankton and three zooplankton functional groups. The influence of the community
99 is represented in the biogeochemical processes in water columns and sediments and eventually be reflected in the bottom DO
100 variability.

101 **2 Methods**

102 **2.1 Coupled hydrodynamic–biogeochemical model**

103 We adapted the three-dimensional, free-surface, topography-following community model, the Regional Ocean Model System
104 (ROMS, version 3.7), on the platform of Coupled Ocean–Atmosphere–Wave–Sediment Transport (COAWST) modeling
105 system (Warner et al., 2010) to the GoM (Gulf–COAWST). ROMS solves finite difference approximations of Reynolds
106 Averaged Navier–Stokes equations by applying hydrostatic and Boussinesq approximations with a split explicit time-stepping
107 algorithm (Haidvogel et al., 2000; Shchepetkin and McWilliams, 2005, 2009). The biogeochemical model applied is primarily
108 based on the NEMURO developed by Kishi et al. (2007). NEMURO is a concentration-based, lower-trophic-level ecosystem
109 model developed and parameterized for the North Pacific. The original NEMURO model has 11 concentration-based state
110 variables, including nitrate (NO_3), ammonium (NH_4), small and large phytoplankton biomass (PS and PL), small, large, and
111 predatory zooplankton biomass (ZS, ZL, and ZP), particulate and dissolved organic N (PON and DON), particulate silica
112 (Opal), and silicic acid ($\text{Si}(\text{OH})_4$). NEMURO is known for its capability to distinguish ZS, ZL, and ZP and to provide a detailed
113 analysis of the dynamics of different functional groups. It was widely used in studies of plankton biomass on regional scales
114 (Fiechter and Moore 2009; Gomez et al., 2018; Shropshire et al., 2020). The embedded Si cycle permits the inclusion of a
115 diatom group (i.e., PL), the dominant phytoplankton group in the nGoM.

116 **2.2 Model modification**

117 In a recent effort, Shropshire et al. (2020) adapted and modified NEMURO to the GoM with five structural changes. (1) The
118 grazing pathway of ZL on PS was removed since, in the GoM, the PS group is predominated by cyanobacteria and
119 picoeukaryotes, which are too small for direct feeding by most mesozooplankton (i.e., ZL). (2) Linear function of mortality
120 was applied for PS, PL, ZS, and ZL, while quadratic mortality was used for ZP, accounting for predation pressure of unmodeled
121 predators, like planktivorous fish. (3) The ammonium inhibition term in the nitrate limitation function was no longer considered
122 exponentially but followed the parameterization by Parker (1993). (4) Light limitation on photosynthesis was replaced with
123 Platt et al.'s (1980) functional form, which was also implemented in the newer version of NEMURO. (5) Constant C: Chl ratio
124 was replaced with a variable C: Chl model according to the formulation by Li et al. (2010).

125

126 However, neither the modified (Shropshire et al., 2020) nor the original (Kishi et al., 2007) NEMURO model considered P
127 and oxygen cycles. In this study, we introduced a P cycle into NEMURO, including three concentration-based state variables
128 as phosphate (PO_4), particulate organic P (POP), and dissolved organic P (DOP). The P limitation on phytoplankton growth

129 was introduced using the Michaelis–Menten formula. In the NEMURO model, N serves as the common “currency”, while P
 130 and Si are converted to N using the Redfield ratio of P: N: Si=1: 16: 16. In the river-dominated LaTex shelf, inorganic and
 131 organic nutrients are supplied mainly by rivers. In our model, riverine PO₄ (Fig. C1), DOP, and POP were prescribed based on
 132 water quality measurements at river gages. When no measurement was available, the PO₄, DOP, and POP were approximated
 133 using total nitrate+nitrite (NO₃+NO₂), dissolved organic N (DON), and particulate organic N (PON) measurements,
 134 respectively, via the Redfield ratio of P: N=1: 16. We neglected the POP settling process but preserved these pools by
 135 introducing the stoichiometric ratio between P and N instead. In other words, the sinking process of POP was implicitly
 136 included by building linkages between PON and POP concentrations, as the sinking of PON was considered in the model.
 137 Governing equations for P state variables were given according to Eqs. 1–3. Please also refer to the appendices for more details
 138 on expressions of modified terms (Appendix A), state variables (Appendix Table B1), source and sink terms (Appendix Table
 139 B2), and values of parameters (Appendix Table B4).

$$\begin{aligned}
 141 \quad \frac{d(PO_4)}{dt} &= (ResPSn + ResPLn) \cdot RPO4N \\
 142 \quad &+ (DecP2N + DecD2N) \cdot RPO4N \\
 143 \quad &+ (ExcZSn + ExcZLn + ExcZPn) \cdot RPO4N \\
 144 \quad &- (GppPSn + GppPLn) \cdot RPO4N,
 \end{aligned} \tag{1}$$

$$\begin{aligned}
 145 \quad \frac{d(DOP)}{dt} &= (DecP2D - DecD2N) \cdot RPO4N \\
 146 \quad &+ (ExcPSn + ExcPLn) \cdot RPO4N,
 \end{aligned} \tag{2}$$

$$\begin{aligned}
 147 \quad \frac{d(POP)}{dt} &= (MorPSn + MorPLn + MorZSn + MorZLn + MorZPn) \cdot RPO4N \\
 148 \quad &+ (EgeZSn + EgeZLn + EgeZPn) \cdot RPO4N \\
 149 \quad &- (DecP2N + DecP2D) \cdot RPO4N,
 \end{aligned} \tag{3}$$

150 We further adapted the oxygen cycle developed by Fennel et al. (2006, 2013) to NEMURO for hypoxia simulations. However,
 151 our model's biogeochemical processes are slightly different due to the different plankton functional groups considered. Sources
 152 for oxygen are contributed by the photosynthesis of two phytoplankton functional groups, while the sinks are attributed to
 153 respirations of two phytoplankton functional groups, metabolism of three zooplankton functional groups, light-dependent
 154 nitrification (Olson, 1981; Fennel et al., 2006), aerobic decomposition of particulate and dissolved organic matter (measured
 155 as PON, and DON, respectively), and SOC. Wanninkhof's (1992) parameterization was implemented for estimates of oxygen
 156 air–sea flux. The biogeochemical dynamics of oxygen were adopted as follows (Eq. 4; also see detailed descriptions of
 157 variables and parameters in Appendix A–B):

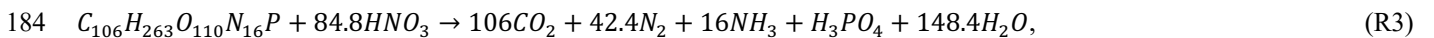
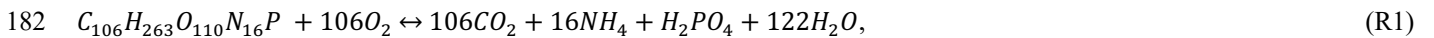
$$\begin{aligned}
 158 \quad \frac{d(Oxyg)}{dt} &= (rOxNO_3 \cdot GppNPS + rOxNH_4 \cdot GppAPS) \\
 159 \quad &+ (rOxNO_3 \cdot GppNPL + rOxNH_4 \cdot GppAPL)
 \end{aligned}$$

$$\begin{aligned}
161 & -ResPSn \cdot [RnewS \cdot rOxNO_3 + (1 - RnewS) \cdot rOxNH_4] \\
162 & -ResPLn \cdot [RnewL \cdot rOxNO_3 + (1 - RnewL) \cdot rOxNH_4] \\
163 & -rOxNH_4 \cdot (ExcZSn + ExcZLn + ExcZPn) \\
164 & -2 \cdot Nit \cdot LgtlimN \cdot \hat{r} \\
165 & -rOxNH_4 \cdot (DecD2N + DecP2N) \cdot \hat{r} \\
166 & -SOC \cdot THK_{bot}, \tag{4}
\end{aligned}$$

167 A PON_{sed} pool due to vertical sinking processes of PON was introduced for parameterization of SOC. The SOC scheme (Fennel
168 et al., 2006) is known as the instantaneous consumption of DO. As soon as the PON falls into the sediment bed, PON will be
169 decomposed instantaneously. This scheme tends to underestimate SOC at the peak of blooms and to overestimate SOC after
170 blooms since the lag in SOC demand is neglected (Fennel et al., 2013). We considered such temporal delays in SOC by
171 introducing a PON_{sed} pool. A portion of sinking PON ends up with PON_{sed} , while the rest is buried (PON_{burial}) and is removed
172 from the system. The parameterization is shown in the following. 1) Organic matter settling down at the conceptual sediment
173 layer is remineralized at a temperature-dependent aerobic remineralization rate, K_{P2N} . 2) Sediment oxygen is consumed only
174 in the oxidation of sedimentary organic matter (represented by PON_{sed}) and the nitrification of ammonium to nitrate (Fennel
175 et al., 2006). 3) Oxygen consumption at the conceptual sediment layer directly contributes to oxygen concentration decreases
176 only at the bottom water column. 4) Sediment denitrification is linearly related to SOC according to observational-based
177 estimates by Seitzinger and Giblin (1996), but the relationship was modified by Fennel et al. (2006) with a slightly smaller
178 slope of denitrification on SOC rate, i.e.,

$$179 \text{denitrification} (mmolN m^{-2} day^{-1}) = 0.105 \times SOC (mmolO_2 m^{-2} day^{-1}), \tag{5}$$

180 5) Aerobic decomposition of PON_{sed} , sediment nitrification, and denitrification follow chemical equations according to
181 (Fennel et al., 2006):



185

186 6) Nitrate produced in sediments (Eq. R2) is used for denitrification (Eq. R3). The linear assumption in 4) implicitly builds
187 relationships among the reactions listed in assumption 5). Let's assume that the production rate of NH_4 by aerobic
188 decomposition (Eq. R1) of organic matter is $M \text{ mmol m}^{-3} \text{ day}^{-1}$, and that the fraction of denitrification-produced CO_2 (Eq. R3)
189 to the total CO_2 production (Eqs. R1 and R3) is x . According to the linear assumption abovementioned, the consumption rate
190 of NO_3 during denitrification (Eq. R3) is proportional to the total consumption rate of O_2 in the sediment (Eqs. R1 and R2),

191 yielding $\frac{84.8Mx}{16(1-x)} = 0.105 \times \left[\frac{106M}{16} + \frac{84.8Mx}{8(1-x)} \right]$ and further $x \approx 0.1425$. The oxygen consumption rate (Eq. 6) and organic matter

192 consumption rate (Eq. 7) due to the coupled aerobic decomposition, nitrification, and denitrification processes can be obtained
 193 by substituting the x value into the stoichiometric ratios according to Eqs. R1–R3.

$$194 \quad Oxyg_{consumption} = \frac{106M}{16} + \frac{84.8Mx}{8(1-x)} = 8.3865M, \quad (6)$$

$$195 \quad OM_{consumption} = \frac{M}{16} + \frac{Mx}{16(1-x)} = 0.0729M, \quad (7)$$

196 Accordingly, the SOC and consumption rate of PON_{sed} are given, respectively as follows:

$$197 \quad SOC = Oxyg_{consumption} \cdot THK_{bot} = 8.3865M \cdot THK_{bot}, \quad (8)$$

$$198 \quad PON_{sedconsumption} = 16 \cdot OM_{consumption} \cdot THK_{bot} = 1.1662M \cdot THK_{bot}, \quad (9)$$

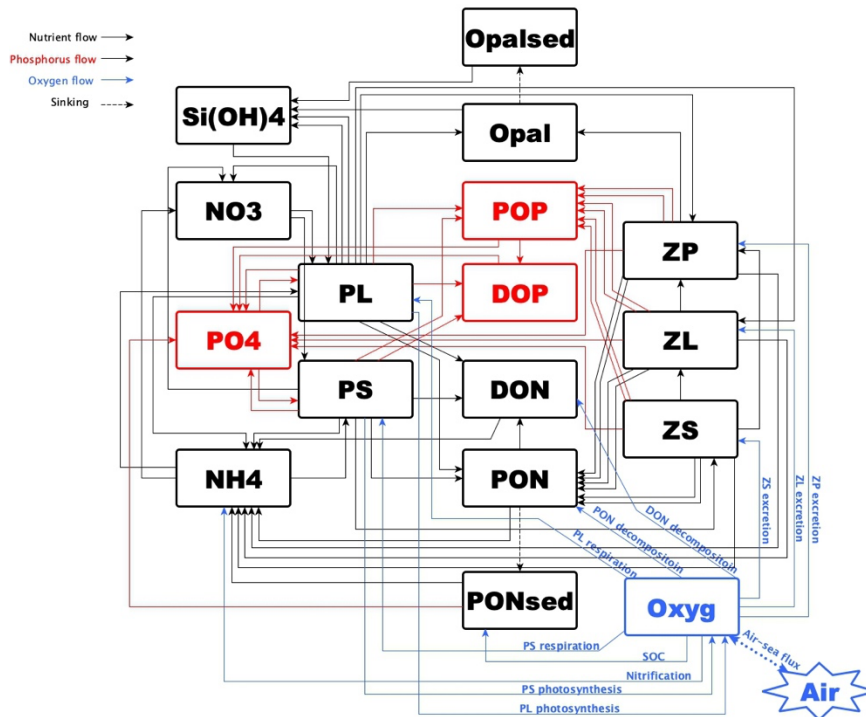
199 where,

$$200 \quad M = \frac{PON_{sed} \cdot VP2N_0 \cdot \exp(K_{P2N} \cdot TMP)}{THK_{bot}}, \quad (10)$$

$$201 \quad THK_{bot} = \text{thickness of bottom water column}, \quad (11)$$

202

203 We further added light inhibition on the nitrification (Olson, 1981) and oxygen dependency on nitrification and aerobic
 204 decomposition. These parametrizations were applied following descriptions by Fennel et al. (2006, 2013). For the oxygen-
 205 dependent term, an oxygen threshold was specified below which no aerobic respiration or nitrification occurred. Detailed
 206 equations were listed in Appendix A. The structure of the newly modified NEMURO model was shown in a schematic diagram
 207 in Fig. 1.



208

209 **Figure 1. Schematic diagram of the modified NEMURO model. Note that the P flow and the oxygen flow are two newly added flows**
210 **to the original NEMURO model.**

211 **2.3 Model set-ups**

212 The coupled model was applied to the GoM using Arakawa C-grid with a horizontal resolution of ~5 km (Fig. 2a). There are
213 334 and 357 interior rho points in the east-west and north-south directions, respectively. The model includes 36 sigma layers
214 vertically. The wetting and drying scheme (Warner et al., 2013) was implemented for a more accurate representation of shallow
215 water. The computational time step (i.e., baroclinic time step) was set to 240 seconds while the number of barotropic time
216 steps between each baroclinic time step was set to 30. Model hindcast was carried out from 1 August 2006 to 26 August 2020
217 with the first 5 months as a spin-up period. Model results were output on a daily interval at UTC 00: 00.

218

219 The physical model set-ups largely followed an earlier Gulf–COAWST application (Zang et al., 2018, 2019, 2020). Open
220 boundaries were set at the south and east forced by daily water level, horizontal components of 3-D current velocity, horizontal
221 components of depth-integrated current velocity, 3-D water salinity, and 3-D water temperature derived from the Hybrid
222 Coordinate Ocean Model (HYCOM) global analysis products (Bleck and Boudra, 1981; Bleck, 2002) with data assimilated
223 via the Navy Coupled Ocean Data Assimilation system (Cummings, 2005; Cummings and Smedstad, 2013; Fox et al., 2002;
224 Helber et al., 2013). For lateral boundary conditions, we utilized Chapman implicit for free surface and water level (Chapman,
225 1985), Flather for depth-integrated momentum (Flather, 1976), gradient for mixing total kinetic energy, and mixed radiation-
226 nudging conditions for 3-D momentum, temperature, and salinity (Marchesiello et al., 2001). The nudging time steps for the
227 mixed radiation-nudging condition were set to 1 day for inflows and 30 days for outflows. The boundary nudging technique
228 was performed at the computational grids along the open boundary. The boundary condition types for passive biological and
229 chemical tracers (i.e., PS, PL, ZS, ZL, ZP, NO₃, NH₄, PON, DON, Si(OH)₄, opal, PO₄, POP, DOP, and Oxyg) were all
230 prescribed as radiation.

231

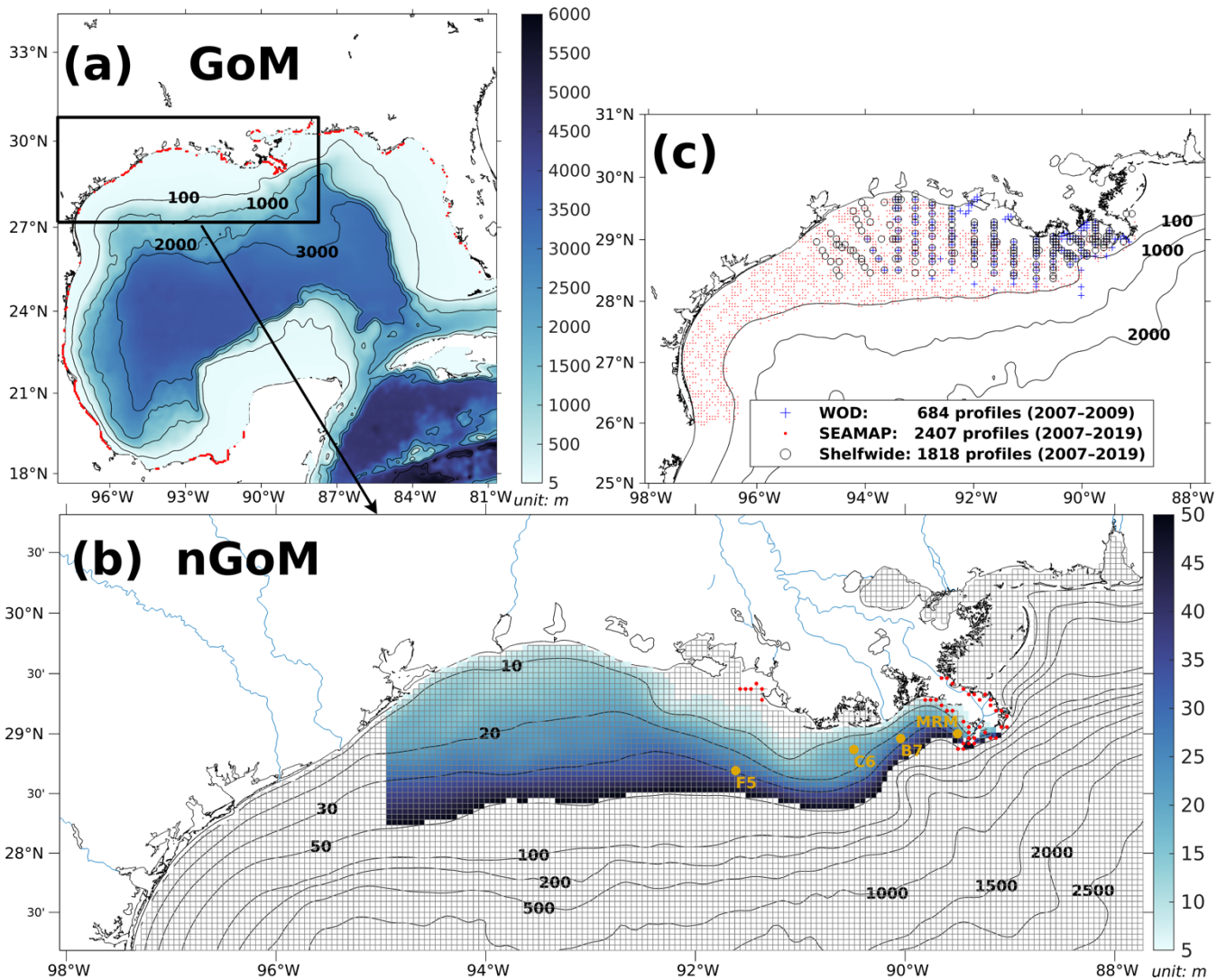
232 Initial conditions for water level, horizontal components of 3-D current velocity, horizontal components of depth-integrated
233 current velocity, 3-D water salinity, and 3-D water temperature were provided by the same HYCOM products as well. Initial
234 conditions for concentrations of NO₃, PO₄, and Si(OH)₄ were interpolated from measurements provided by the World Ocean
235 Database (WOD, Boyer et al., 2018). Initial conditions for DO concentration were given by World Ocean Atlas (WOA, Garcia
236 et al., 2018). At the sediment layer, PON_{sed}, PON_{burial}, opal_{sed}, and opal_{burial} were initialized as 0.1 mmol m⁻³. Other biological
237 and chemical tracers were initialized as 0.1 mmol m⁻³ due to the lack of observations.

238

239 Atmospheric forcings, including surface wind velocity at 10 m height above sea level, net longwave radiation flux, net
240 shortwave radiation flux, precipitation rate, air temperature 2 m above sea level, sea surface air pressure, and relative humidity
241 2 m above sea level, were derived from the National Centers for Environmental Prediction (NCEP) Climate Forecast System
242 Reanalysis (CFSR) 6-hourly products (for years prior to 2011, Saha et al., 2010) and NCEP CFS Version 2 (CFSv2) 6-hourly

243 products (for years starting from 2011, Saha et al., 2011) with a horizontal resolution of ~35 km and ~22 km, respectively. In
244 our model, 63 rivers were considered as horizontal point source forcings along the coastal GoM. They were split into 280
245 points (red dots in Fig. 2a) sources transporting time-varying salinity (nearly zero), temperature, 3-D horizontal momentum
246 (based on the magnitude of river discharges), nutrients (NO_3 , NH_4 , PO_4 , $\text{Si}(\text{OH})_4$, PON, DON, POP, and DOP; Fig. C1), and
247 DO to the computational domain. Locations of river point sources of the Mississippi and the Atchafalaya Rivers were shown
248 as red dots in Fig. 2b. For reconstructions of time series of river forcing terms, we composed measurements from various
249 sources, including U.S. Geological Survey (USGS) National Water Information System (NWIS), National Oceanic and
250 Atmospheric Administration (NOAA) Tides and Currents System (TCS), NOAA National Estuarine Research Reserve System
251 (NERRS), and Mexico National Water Commission (CONAGUA, for rivers in Mexico's territory). Daily averaged river
252 discharges were given based on measurements by USGS NWIS and CONAGUA. The magnitude of river discharges was
253 multiplied by 1.4 to account for adjacent watershed areas and the lateral inflow of tributaries (Warner et al., 2005). River
254 temperature and salinity time series were reconstructed from measurements by USGS NWIS, NOAA TCS, and NOAA
255 NERRS. River nutrient concentrations were provided monthly by USGS NWIS and NOAA NERRS and were extended to
256 daily time series with values in the corresponding months. Riverine DO concentration was set to be a constant (258 mmol m^{-3})
257 assuming that riverine DO was saturated at 25 °C under 1 atm. Besides, tidal forcings were introduced in the hydrodynamic
258 model taking into account of influences of tidal elevations and tidal currents. There were 13 tidal constituents considered in
259 the model including M2, S2, N2, K2, K1, O1, P1, Q1, MF, MM, M4, MS4, and MN4.

260



261
 262 **Figure 2.** (a) Bathymetry of the entire domain of the Gulf–COAWST, (b) zoom-in bathymetry plot of the northern Gulf of Mexico
 263 (nGoM), and (c) locations of observed inorganic nutrient and DO profiles derived from WOD, SEAMAP, and NOAA’s shelf-wide
 264 cruises. In (a), locations of river point sources are denoted by red dots. In (b), only bathymetry between 6 and 50 m was mapped
 265 with colors; computational meshes were split by solid grey lines; main river channels are denoted by solid blue curves; locations of
 266 river point sources of the Mississippi and the Atchafalaya Rivers are indicated by red dots; sampling locations for SOC and
 267 overlaying water respiration measurements by McCarthy et al. (2013) are denoted by dark yellow dots.

268 3 Biogeochemical model validations

269 3.1 Available measurements

270 In this section, biogeochemical model validations were conducted for inorganic nutrient concentration profiles (i.e., NO_3 , PO_4 ,
 271 and $\text{Si}(\text{OH})_4$), ratios of diatom and total phytoplankton, SOC, DO concentration profiles, spatial distributions of bottom DO

272 concentration, and temporal variability of the hypoxic area against multiple field and lab data sets. Validation of the
273 hydrodynamic model can be found in Zang et al. (2019).

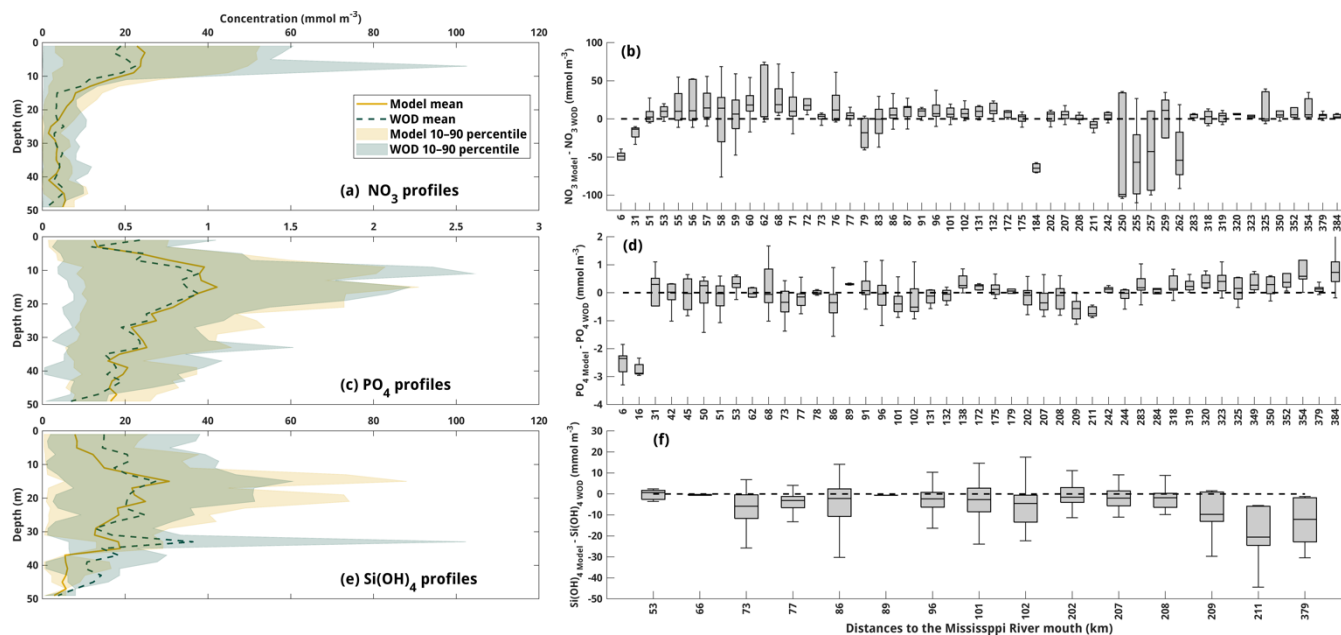
274

275 Inorganic nutrient concentration profiles from WOD were used for model validation. WOD measurements cover the period
276 from 11 January 2007 to 5 July 2009 including 478 NO_3 profiles, 409 PO_4 profiles, and 217 $\text{Si}(\text{OH})_4$ profiles. The diatom
277 percentage of total phytoplankton was derived from measurements by Chakraborty and Lohrenz (2015) and Schaeffer et al.
278 (2012). The SOC measurements were from an incubation study (McCarthy et al., 2013). Available DO concentration profiles
279 were obtained from the NOAA-supported mid-summer shelf-wide cruises and Summer Groundfish Survey in GoM supported
280 by Southeast Area Monitoring and Assessment Program (SEAMAP) conducted annually by the Gulf States Marine Fisheries
281 Commission. The shelf-wide cruises provided 1818 measured profiles with 85140 available records from 2007 to 2019. There
282 were at least 83 DO profiles for each summer (June–August, except 2016) from the shelf-wide cruise observations. The
283 selected SEAMAP DO dataset covers a time range from 2007 to 2019 with measurements including 2407 profiles with 77415
284 sampled records. Locations of the selected profiles from different archives were shown in Fig. 2c. Summer measurements by
285 the shelf-wide cruises were used to validate spatial patterns of bottom DO concentration and time series of summer hypoxic
286 areas. Estimated hypoxic areas by the cruises are available from 2007 to 2020 with a range from 5,480 km^2 to 22,720 km^2 .

287 **3.2 Nutrients concentration profiles**

288 Modeled results showed good agreements with WOD nutrient profiles (Fig. 3a, 3c, and 3e, averaged every 2 m from the surface
289 to 50 m depth) in terms of vertical distribution and magnitudes. The surface waters were rich in NO_3 (Fig. 3a) but oligotrophic
290 in PO_4 (Fig. 3c) and $\text{Si}(\text{OH})_4$ (Fig. 3e), indicating possibly high diatom productivity (Table 1) and possible P or Si limitation
291 in the photic zone. Previous numerical studies did not provide comparisons for nutrient profiles in the shallow LaTex shelf
292 region but focused more on the validation for surface nutrient concentration. Although surface nutrients are important for
293 plankton blooms, the nutrient concentration at other water layers is also critical in affecting the shelf production dynamics.
294 The simulated profiles were linearly interpolated to the observed depth for point-to-point comparisons. Biases were
295 summarized and shown against the distance to the Mississippi River mouth (Fig. 3b, 3d, and 3f). An overall overestimation of
296 NO_3 was found, especially around the mouths of the Mississippi River (distances < 70 km), where most of the biases were
297 between $\pm 50 \text{ mmol m}^{-3}$. Biases around the Atchafalaya River mouth (distances between 250 to 260 km) were detected
298 negatively with a wider range than that around the Mississippi River mouth. In other locations, most NO_3 biases are within \pm
299 25 mmol m^{-3} . There is no pronounced overestimation or underestimation detected for the PO_4 biases, which are mostly within
300 $\pm 1 \text{ mmol m}^{-3}$, except for waters around the Mississippi River mouth. The PO_4 biases ranged from -3 to -2 mmol m^{-3} for profiles
301 close to the mouth (distances < 16 km). Slight underestimation was found in the $\text{Si}(\text{OH})_4$ concentration biases, especially for
302 profiles around the Atchafalaya River mouth (distances = 211 km). Most of the $\text{Si}(\text{OH})_4$ biases ranged from -20 to 5 mmol m^{-3}
303 and were smaller than the magnitude of the NO_3 biases. Mean NO_3 concentrations from the Mississippi and Atchafalaya
304 Rivers were $99 \pm 34 \text{ mmol m}^{-3}$ (mean $\pm 1\text{sd}$) and $66 \pm 29 \text{ mmol m}^{-3}$, respectively. Mean riverine PO_4 concentrations were 2.7

305 $\pm 0.7 \text{ mmol m}^{-3}$ and $2.3 \pm 0.7 \text{ mmol m}^{-3}$, respectively, and mean riverine Si(OH)_4 concentrations were $118 \pm 23 \text{ mmol m}^{-3}$ and
 306 $116 \pm 21 \text{ mmol m}^{-3}$, respectively. The nutrient concentrations bias between simulations and observations is acceptable,
 307 considering the possible transient influence from the riverine nutrient loads during a survey.



308
 309 **Figure 3. Profile comparisons between model hindcasts and WOD measurements for concentrations of (a)–(b) NO_3 , (c)–(d) PO_4 , and**
 310 **(e)–(f) Si(OH)_4 . Box charts on the right-hand side show the minimums, maximums, first quartiles, third quartiles, and medians of**
 311 **the concentration differences between the hindcast and measured profiles.**

312 3.3 Diatom ratios

313 Both measured and model-simulated Si(OH)_4 profiles suggested strong diatom productivity in the photic zone (Fig. 3e). Cruise
 314 observations confirmed that the LaTex phytoplankton community is dominated by the diatom group (Schaeffer et al., 2012;
 315 Chakraborty and Lohrenz, 2015). Regional averages (Fig. C2 in Appendix C), vertical averages (only the surface, middle, and
 316 bottom layers were chosen), and monthly averages were applied to the concentration ratio of diatom and total phytoplankton
 317 according to the sampled locations, sampled layers, and sampled months, respectively, of the cruise studies by Schaeffer et al.
 318 (2012) and Chakraborty and Lohrenz (2015). The modeled ratios well reproduced the measured ones in terms of magnitudes,
 319 monthly variability, and cross-shelf variability (Table 1). During the cruise periods in 2008, the range of modeled diatom
 320 percentage (79% to 99%) matched well with the measurements (79% to 88%) except for June 2008, when underestimations
 321 were found. In 2009, our model results agreed well with the measurements in inner shelf waters but overestimated the
 322 measurements in the mid-shelf regions, especially in the summer and fall of 2009. The measured percentages exhibited salient
 323 monthly variations with higher values in winter and spring and low ones in summer and fall. In the cross-shelf direction, the
 324 phytoplankton community shifted from a highly diatom-dominated one in the inner shelf waters to a less diatom-dominated
 325 one in the mid-shelf waters, especially in summer. Such patterns were well captured by our model.

327 **Table 1. Comparison of simulated (mean \pm 1SD) and measured (mean \pm 1SD in parentheses) diatom percentage of the total**
 328 **phytoplankton. Note that the statistics for the simulated percentages were conducted based on concentration values and averaged**
 329 **over the cruise months and over given regions that cover the cruise sampling locations (Fig. C2). The measured percentages by**
 330 **Schaeffer et al. (2012) (for measurements in 2008) were calculated based on biovolume values, while those by Chakraborty and**
 331 **Lohrenz (2015) (for measurements in 2009) were given by chlorophyll *a* attributed to different phytoplankton groups.**

	Diatom/total phytoplankton \times 100%	
	Inner shelf	Midshelf
February 2008	99 \pm 4 (88 \pm 16)	
April 2008	99 \pm 2 (71 \pm 16)	
May 2008	79 \pm 39 (79 \pm 22)	
June 2008	29 \pm 42(85 \pm 10)	
January 2009	60 \pm 29 (66 \pm 21)	57 \pm 14 (47 \pm 14)
April 2009	50 \pm 33 (59 \pm 14)	51 \pm 19 (33 \pm 29)
July 2009	41 \pm 33 (40 \pm 13)	33 \pm 24 (13 \pm 16)
October–November 2009	50 \pm 33 (46 \pm 14)	38 \pm 19(19 \pm 17)
March 2010	49 \pm 35 (50 \pm 14)	52 \pm 26 (64 \pm 12)

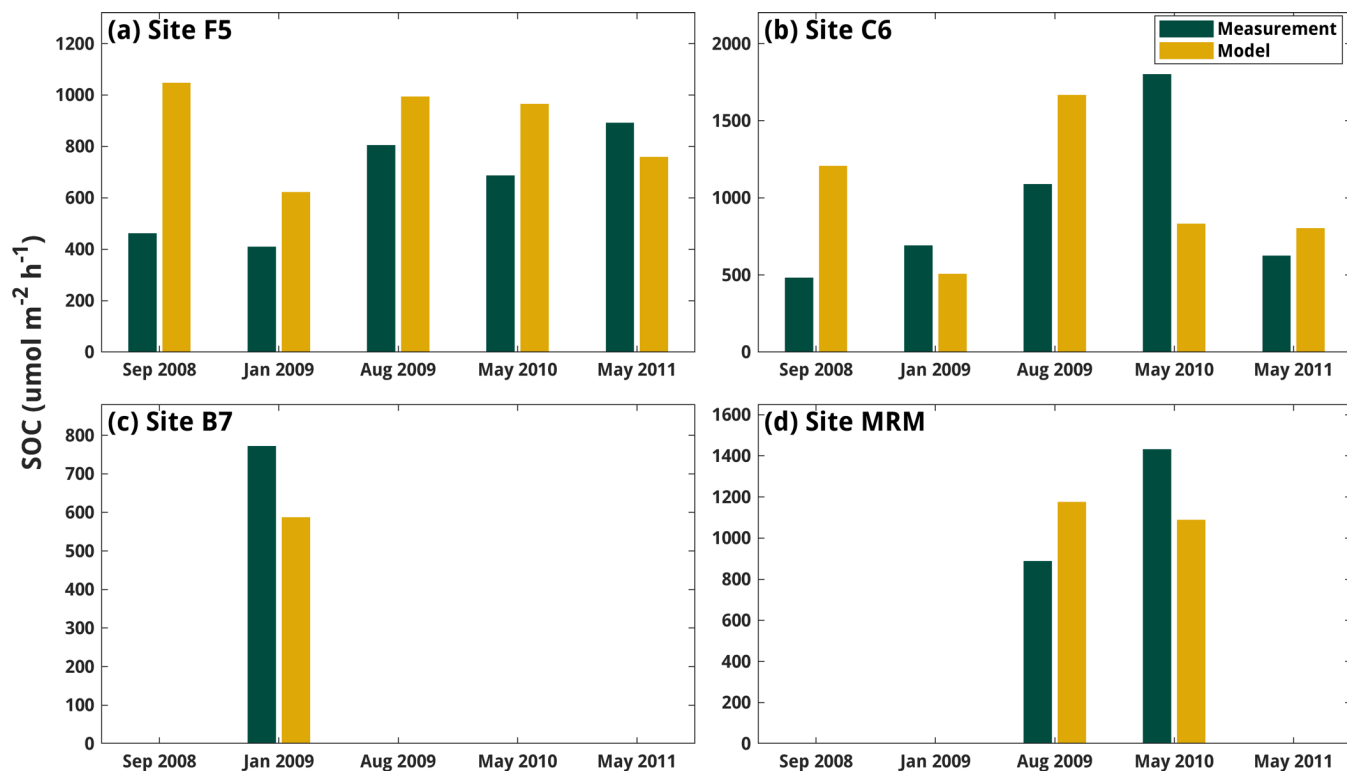
332

333 3.4 SOC rates

334 Modeled SOC rates were compared against the laboratory incubation by McCarthy et al. (2013) at five shelf sites (location see
 335 the Fig. 1 in that paper) using sediment and water samples collected during six cruises (i.e., July 2008, September 2008, January
 336 2009, August 2009, May 2010, and May 2011). The modeled SOC was averaged over the cruise months for four shelf sites
 337 (i.e., F5, C6, B7, and MRM; Fig. 2b). Our model could well capture the SOC magnitude. The model generally overestimated
 338 the SOC at sites F5 and C6 except for January 2009 and May 2010 at site C6 and underestimated SOC at sites B7 and MRM
 339 (except for August 2009) (Fig. 4). The largest overestimations were found on September 2008 when measurements were
 340 carried out shortly after Hurricanes Gustav and Ike. These measurements tended to provide a low SOC but a high water column
 341 respiration, possibly induced by the mixing incurred by storms. Note that the model results shown in Fig. 4 were averaged
 342 over an entire month because no exact cruise date information was reported by McCarthy et al. (2013).

343

344

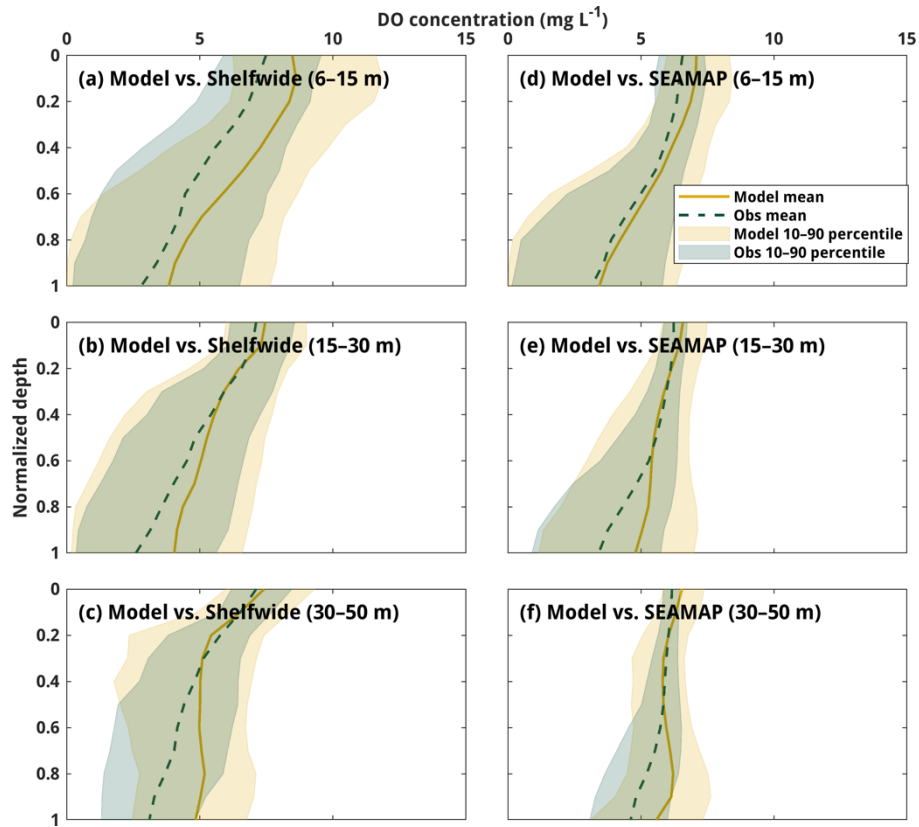


345

346 **Figure 4. Comparison of modeled and measured SOC (unit: $\mu\text{mol m}^{-2} \text{h}^{-1}$) at four LaTex shelf sites (Fig. 2b). Note that the**
 347 **measurements are provided by McCarthy et al.'s (2013) incubation study.**

348 3.5 DO profiles

349 Both simulated and observed DO profiles were averaged for different depth ranges (Fig. 5) and compared against normalized
 350 depths ranging from 0 (surface) to 1 (bottom). The observed DO vertical structures were well captured by the model, with the
 351 10–90 percentiles of modeled DO overlapping the measured ones well. We noticed the model tended to overestimate the
 352 observed DO by $\sim 1 \text{ mg L}^{-1}$ on average, especially in lower water columns for profiles with greater depths, which can be
 353 ascribed to the model's relatively coarse vertical resolution in deeper waters. The vertical coordinate transformations and
 354 vertical stretching functions applied to the model provided a finer resolution around the surface and relatively coarse ones
 355 around the bottom (1 to 2 m for each layer), while the shelf-wide and SEAMAP measurements were almost equally distributed
 356 along the vertical direction. We noted our model was less biased against the SEAMAP than the shelf-wide data as the latter
 357 sometimes has several measurements within one meter. In shallow waters (6–15 m), DO was somewhat more overestimated
 358 around the surface than in layers below (Fig. 5a and 5d). ROMS tends to overmix the water column in shallow water regardless
 359 of the vertical mixing parameterizations chosen (Robertson and Hartlipp, 2017). Despite the slight overestimations of DO
 360 profiles, our model results provided similar and even better performances than previous numerical studies. For example, DO
 361 concentration biases against profile measurements in Yu et al. (2015) were within 2 mg L^{-1} .



362

363 **Figure 5. Comparisons of DO profiles between model hindcasts and measurements by (a–c) NOAA’s shelf-wide cruises and (d–f)**
 364 **SEAMAP. The normalized depths of 0 and 1 represent the surface and bottom, respectively.**

365

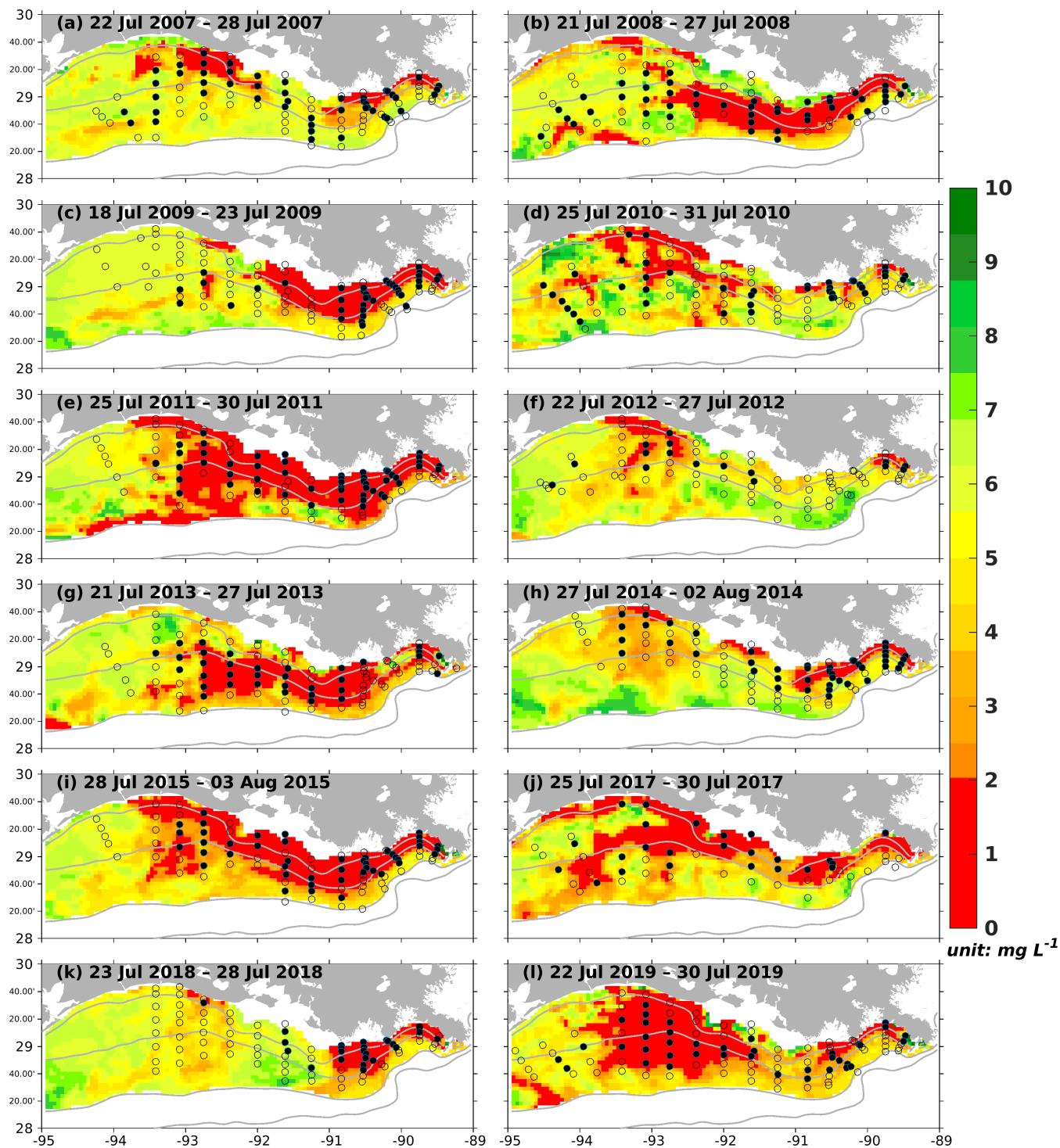
366 3.6 Spatial distributions of bottom DO and temporal variability of hypoxic area

367 As the annual NOAA shelf-wide cruises were conducted from the east shelf to the west in the summer, the model simulated
 368 bottom DO was resampled following the cruise periods. For example, if the westmost location of the cruise is 90°W on day 1,
 369 the simulated bottom DO concentration over the east of 90°W on that day is extracted. On the following day, if the westmost
 370 location of the cruise is 91°W, the simulation between 91°W and 90°W on day 2 is extracted, and so forth. All the extracted
 371 frames were blended to reconstruct the spatial distribution of simulated bottom DO concentration during the summer cruise
 372 period. Simulated results outside the LaTex shelf and over the deep (> 50 m) and shallow (< 6 m) water regions were excluded
 373 since observations were unavailable. Model results showed a good agreement with the observations in terms of interannual
 374 variability and spatial extent of bottom hypoxic waters (Fig. 6). The spatial distribution of the hypoxic regions varied over
 375 different summers. For example, the hypoxic area was small and was primarily restricted to nearshore (<20 m) regions during
 376 the summers of 2007, 2009, 2010, 2012, 2014, and 2018. The size of the hypoxic zone was more prominent and extended
 377 offshore in 2008, 2011, 2013, and 2019. The spatial dispersion of hypoxic waters occurred mostly over the west of the LaTex

378 shelf, where bathymetry gradients were gentle. Over the eastern shelf, the hypoxic water was mostly constrained within a
379 narrow belt. In the meantime, the western and eastern hypoxic waters were not always merged but were separated at around
380 91 °W (e.g., 2007, 2010, 2012, 2014, 2017, and 2018). These results suggested that the hypoxia development on the LaTex
381 shelf was complex and generally followed the bathymetry and distances from the major river mouths.

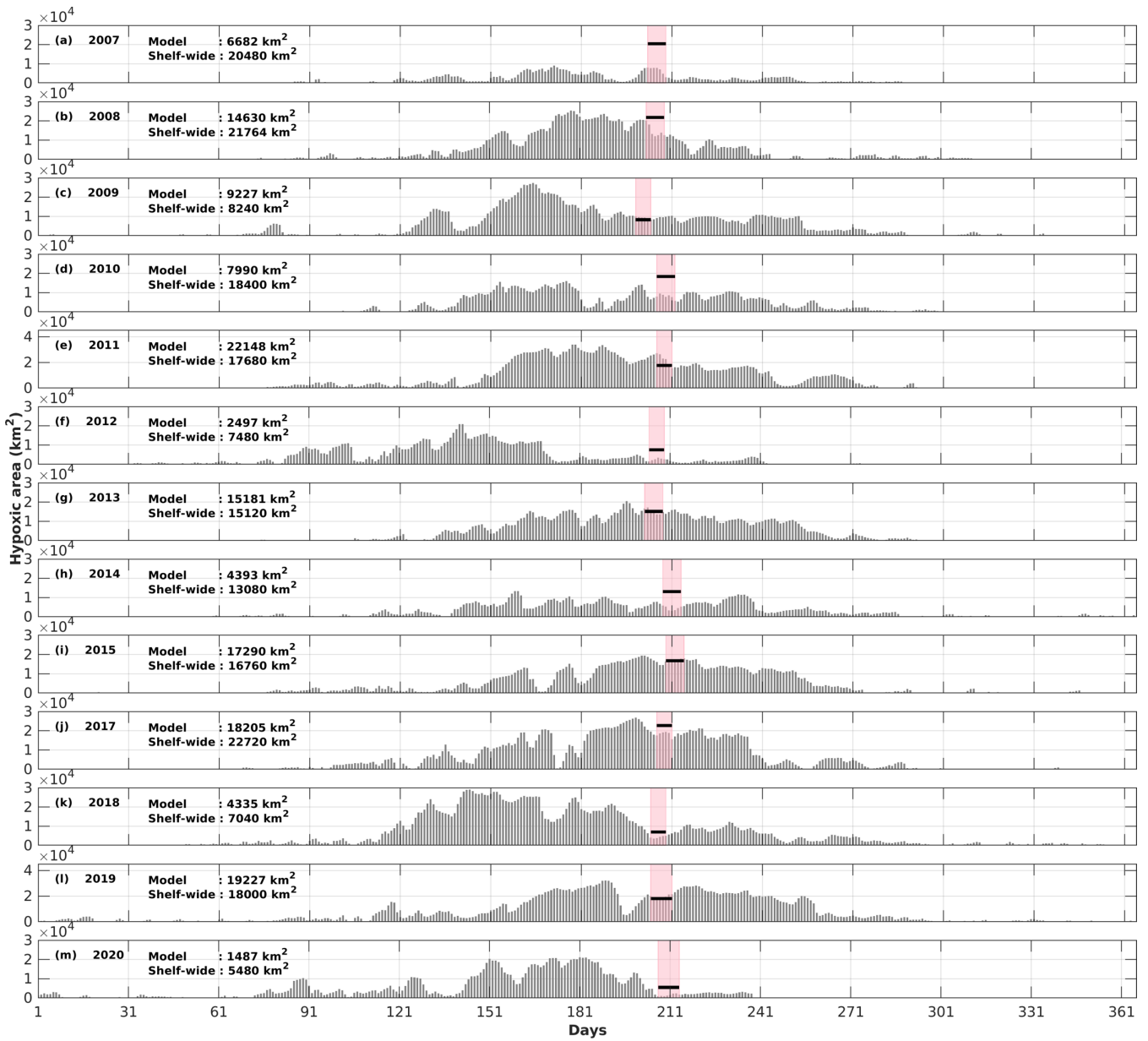
382

383 The daily time series of the size of the hypoxic zone was calculated over the LaTex shelf (6–50 m; Fig. 7). There was a good
384 agreement between simulated hypoxia zone size and that captured by the shelf-wide cruises in terms of variability and
385 magnitude. The overall R^2 was found as 0.47 and varied yearly (Table 2). The 5-year running R^2 increased from 0.02 for the
386 first 5-year period (2007–2010) to 0.91 for the last 5-year period (2015–2020, excluding 2016). The lower R^2 before 2010
387 could be attributed to the coarse resolution of the atmospheric forcings (~ 35 km, CFSR). Since 2011, CFSRv2 provided
388 forcings with a higher resolution of 22 km. Underestimations were found in 2007, 2010, 2012, and 2014 with a root-mean-
389 squared error (RMSE) of 9988 km², while minor underestimations were simulated in 2008, 2017, 2018, and 2020 (RMSE=4862
390 km²). The model tended to slightly overestimate the measurements in other summers of interest (i.e., 2009, 2011, 2013, 2015,
391 and 2019; RMSE=2132 km²). Nevertheless, those biases were acceptable considering the relative sporadic converges of cruise
392 data.



393

394 **Figure 6. Modeled summer bottom DO concentration (colored patches) and NOAA's summer shelf-wide hypoxia observations (black**
 395 **dots and open circles). The black dots and the open circles are indicators of observed bottom hypoxia and normoxia, respectively.**
 396 **The solid grey lines indicate bathymetry of 10, 20, 50, and 100 m, respectively.**



397

398 **Figure 7. Comparison of the hypoxic area (in km²) between model simulations and shelf-wide cruise observations from 2007 to 2020**
 399 **(except 2016). The pink patches denote the cruises periods while the solid black lines represent the measured hypoxic area.**

400

401

402

403

404 Table 2. The overall (2007–2020) and 5-year running R^2 of summer hypoxic area between model simulations and shelf-wide
 405 measurements. Note that the comparison in the year 2016 was excluded due to the lack of measurement.

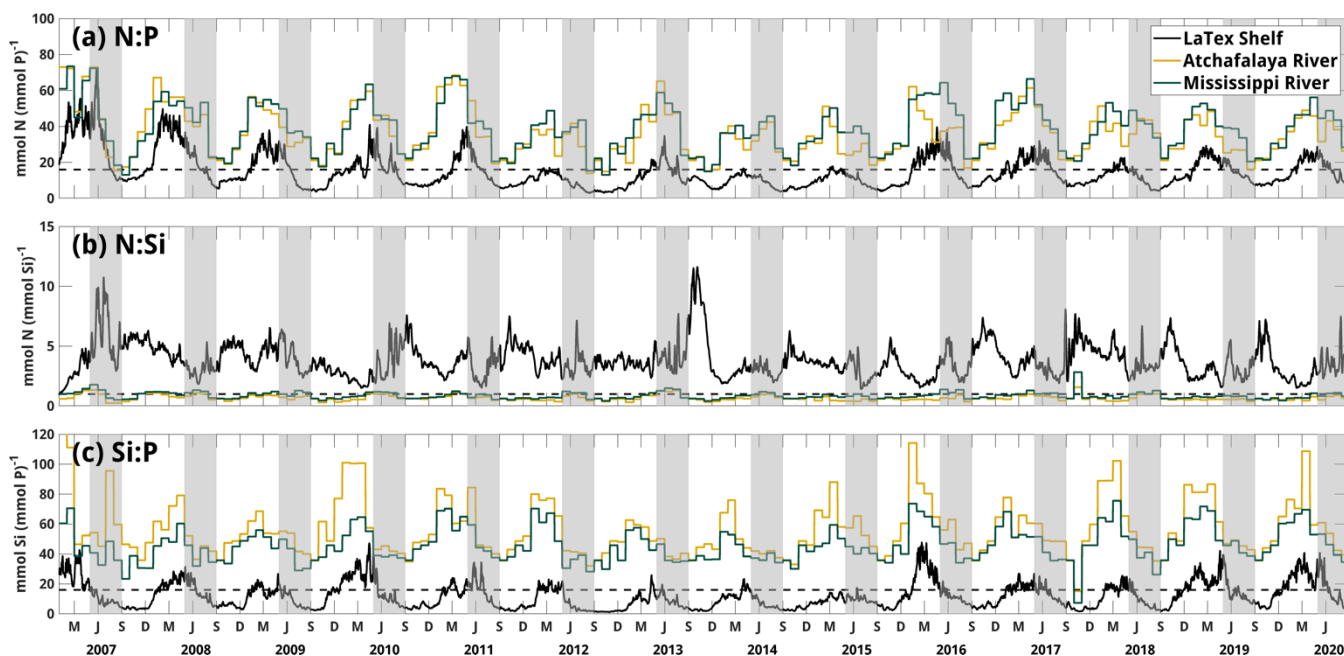
Year ranges	R^2	Year ranges	R^2
2007–2020 (overall)	0.47	2011–2015	0.82
2007–2011	0.02	2012–2017	0.75
2008–2012	0.39	2013–2018	0.71
2009–2013	0.41	2014–2019	0.73
2010–2014	0.44	2015–2020	0.91

406

407 4 Results

408 4.1 Nutrient limitation

409 Riverine nutrient loads from the Mississippi and Atchafalaya Rivers were calculated based on measurements from the USGS
 410 NWIS. During the investigated period (2007–2020), the riverine N:P ratio was higher than 16:1 during spring and reached its
 411 minimum in summer. Riverine N:Si ratio fluctuated around 1:1 and was slightly higher in late spring and summer than in other
 412 seasons (Fig. 8). The rivers transported excessive inorganic N and Si to the shelf but much less P when compared to the
 413 Redfield ratio of N:P:Si=16:1:16. Ratios of integrated nutrient concentration in the shelf (Fig. 8) suggested that P was usually
 414 limited in spring when compared to N and Si. In most summers, Si limitation might be more important in regulating
 415 phytoplankton production than N limitation ($N:Si > 1:1$) and P limitation ($Si:P < 16:1$).



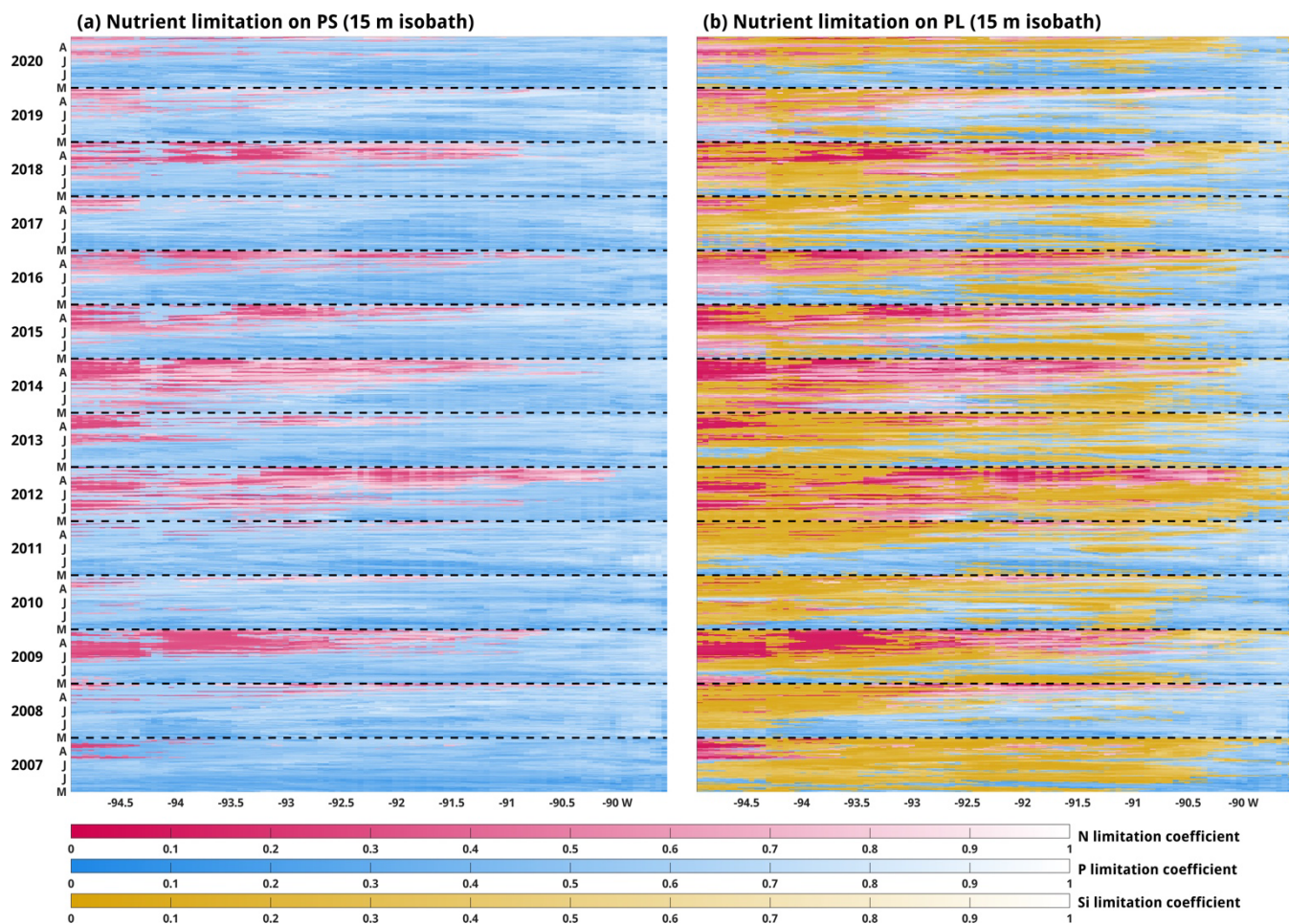
416

417 **Figure 8. Daily time series of ratios of nutrient loads from the Mississippi and Atchafalaya Rivers and nutrient ratios averaged over**
418 **the LaTex shelf (Fig. 2b) from the numerical results. Note that the latter ratios are derived based on the depth-integrated nutrient**
419 **concentrations. The black dashed lines denote the nutrient ratios of 16:1, 1:1, and 16:1 in (a), (b), and (c), respectively. The gray**
420 **patches indicate the late spring and summer (May–August) period of each year. The capitalized letters M, J, S, and D in the x-axis**
421 **denote the first day of March, June, September, and December, respectively.**

422 Nutrient limitation could vary among different phytoplankton species with different efficiencies in nutrient uptakes. In our
423 model, the Si limitation was modeled only for the PL growth. Depth-averaged nutrient limitation coefficients (see Eqs. A9–
424 A10) along multiple isobaths exhibited salient spatial and temporal patterns for both PS and PL (Fig. 9 and C3–C6). For
425 example, along the 15 m isobath (Fig. 9), in the mid and west shelf, the PS growth was usually limited by N in mid- and late
426 summer but by P in other late spring and early summer. In the east shelf, P limitation on PS growth was usually dominated
427 from May to August (Fig. 9a). Types of limited nutrients for PL exhibited a distinguishable west-east pattern along the 15 m
428 isobath: the growth of PL was usually limited by P in the east and by Si in the middle. The limited nutrients shifted between
429 N and Si on the shallow mid and west shelf in different summers. In contrast, P limitation on PS growth and Si limitation on
430 PL growth was likely to be more common in the open shelf (Fig. C3–C6). N limitation was negligible along the 30 m isobath
431 and beyond, where the growth of PS was mostly limited by P and the growth of PL by Si in the west and by P in the east,
432 respectively.

433
434 N limitation was commonly simulated in the shallow (< 20 m) middle and west shelf for the two phytoplankton groups, while
435 in other parts, primary production was more likely to be limited by P or Si. Bioassays studies by Turner and Rabalais (2013)
436 suggested that phytoplankton biomass was mostly limited by N or by a co-limitation of N and P in high salinity (> 20) waters.
437 In the shallow mid and west part of the shelf, where salinity was usually greater than 20 during summer, model results
438 suggested an N-limited environment, which agreed with the bioassays studies. However, in other parts, regardless of salinity
439 ranges, the system was more limited by P and Si. Previous bioassays studies usually neglected Si effects on production (e.g.,
440 Turner and Rabalais, 2013; Zhao and Quigg, 2014). Quigg et al. (2011) pointed out that P limitation was detected particularly
441 at sites directly adjacent to the Mississippi River plume, while Si limitation was found in four out of eight bioassays where
442 production was limited by nutrients. These measurements supported our model results regarding the importance of P and Si
443 limitation on the shelf primary production.

444



445

446 **Figure 9. Evolution of depth-averaged nutrient limitation coefficients for (a) PS and (PL) along the 15 m isobath during late spring**
 447 **and summer. The notations of M, J, J, and A in the y-axis represent the first day of May, June, July, and August, respectively. Note**
 448 **that a lower (deeper colored) coefficient represents stronger limitations on phytoplankton growth. The dashed black lines indicate**
 449 **the time record on May 1 of each year.**

450 4.2 Plankton community dynamics

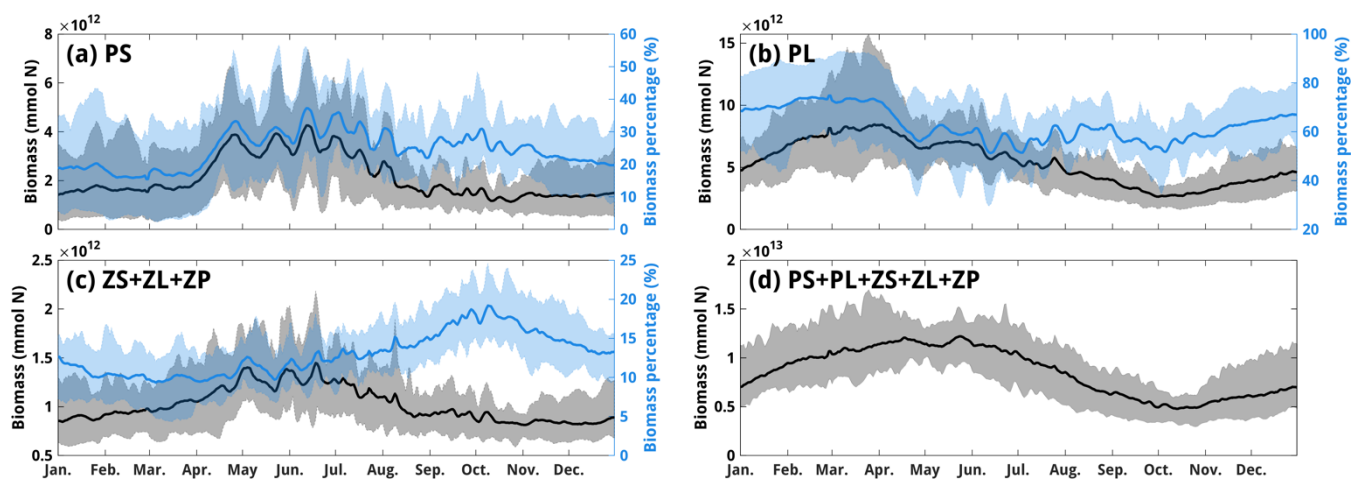
451 As suggested by previous observations (Schaeffer et al., 2012; Chakraborty and Lohrenz; 2015), the LaTex shelf phytoplankton
 452 community is largely supported by the diatom group, which is consistent with our model simulation. Integrated over entire
 453 water columns and the LaTex shelf, the modeled total productions (primary + secondary productions, in mmol N) were
 454 supported mostly by PL, which contributed ~70 % in early spring and ~50 % in summer (Fig. 10b). Contributions from PS
 455 biomass supported ~20 – ~35 % of total biomass from spring to summer (Fig. 10a) when the secondary production (ZS+ZL+ZP)
 456 only contributed ~10 % (Fig. 10c). In the meantime, the seasonality of different biomass subsets exhibited different patterns.
 457 The PS biomass reached its first peak in late April and then varied till July. The PL biomass climbed to its higher peak in early
 458 April, decreased, and rebounded slightly to its lower peak in mid-May. During summer, the PS biomass ($3-4 \times 10^{12}$ mmol N)

459 was at a similar magnitude to the PL biomass ($5\text{--}6 \times 10^{12}$ mmol N). After summer, both PS and PL biomass decreased gradually
 460 to troughs in October. The seasonality of total production, therefore, exhibited a bi-peak (in late spring and early summer)
 461 pattern with the two peaks at a similar magnitude. Such a bi-peak pattern could also be found in both satellite-derived
 462 chlorophyll *a* concentration and model simulations with a similar plankton community as this study (see comparisons of
 463 modeled and satellite chlorophyll *a* concentration in Gomez et al., 2018) but was hardly captured by models using only one
 464 plankton group (e.g., Fennel et al., 2011).

465

466 Competition of PS and PL on nutrients may provide a clue to the bi-peak production. Nutrient loads from the Mississippi and
 467 Atchafalaya Rivers usually maximize in late spring and early summer, after which the loads decrease gradually and reach the
 468 minimum in October (Fig. C1). With greater (Table B4) half-saturation coefficients on nutrients, the PL group outcompetes
 469 the PS group in a high-nutritious environment in April but would not exhibit such superiority in growth in summer when
 470 nutrient supplies decrease. Top-down effects were also detected from the time series of PS and secondary production (Fig. 10a
 471 and 10c). The PS biomass experienced a surge during April and reached its first peak around the end of April, while the
 472 secondary production did not see a salient increase until mid-April and climbed to the highest at the beginning of May. Both
 473 time series then exhibited a pronounced fluctuation after reaching their first peak and declined steadily after August. During
 474 this high-production period, the two time series were out-of-phase with the PS led by about 6 days. There was no
 475 distinguishable phase lag between the seasonality of PL and the secondary production.

476



477

478 **Figure 10.** Climatologically daily mean of (a) PS, (b) PL, (c) ZS+ZL+ZP, and (d) total production. The corresponding percentages
 479 for different biomass subsets are related to the total production and are shown as blue solid lines. The color patches indicate the
 480 range of 10–90 percentiles. Note that the biomass matrices were integrated over the entire water column and the LaTex shelf before
 481 temporal averages.

482

483 We further examined the variance of the daily time series of simulated total productions (4987 records from January 2007 to
 484 August 2020). As the total production was formulated as the sum of productions by PS, PL, ZS, ZL, and ZP, the variance can
 485 be expanded mathematically, as shown in Table 3. The PL explained 63 % of the total variance, while PS explained only 20
 486 %. The daily variability of the shelf production was, therefore, mostly controlled by that of the PL. As Si and P limitations
 487 were commonly found for the growth of phytoplankton (Fig. 9 and C3–C6), more pronounced changes in total production and
 488 the resulting DO concentration would be expected when only adjusting riverine Si or P loads rather than N loads. In the
 489 meantime, the responses in different types of plankton biomass may be different to the changing nutrient loads due to the
 490 competition between PS and PL (bottom-up effects) and also grazing of zooplankton on phytoplankton (top-down effects).
 491

492 **Table 3. The expansion of variance (unit: $\times 10^{22}$ mmol N²) of total production. Note that the sum of the listed variances and**
 493 **covariances is equal to the variances of the total production mathematically. Statistics are derived from the daily time series of**
 494 **plankton biomass (in mmol N) integrated over the entire water column and the LaTex shelf (color-shaded area in Fig. 2b).**
 495 **Percentages in the brackets represent variance contributions.**

var(PS)	var(PL)	var(ZS)	var(ZL)	var(ZP)
216 (20.32 %)	669 (62.97 %)	3.14 (0.30 %)	4.24 (0.40 %)	0.21 (0.02 %)
2cov(PS,PL)	2cov(PS,ZS)	2cov(PS,ZL)	2cov(PS,ZP)	2cov(PL,ZS)
41.6 (3.92 %)	18.6 (1.75 %)	32.2 (3.03 %)	8.86 (0.83 %)	-18.2 (1.71 %)
2cov(PL,ZL)	2cov(PL,ZP)	2cov(ZS,ZL)	2cov(ZS,ZP)	2cov(ZL,ZP)
36.6 (3.45 %)	12.1 (1.14 %)	-0.03 (0.01 %)	0.26 (0.02 %)	1.35 (0.13 %)
sum				
1030				

496 4.3 Plankton contribution to PON_{sed} pool

497 In the model, the PON_{sed} pool is supported by sinking organic matters (represented by PON), which are contributed directly
 498 from plankton detritus due to phytoplankton and zooplankton mortality and zooplankton egestion. Although PL biomass
 499 dominated total production, the daily variability of PON_{sed} was more correlated to the PS and secondary production, with
 500 correlation coefficients of 0.64 ($p < 0.001$) and 0.70 ($p < 0.001$), respectively, than to the PL, with a coefficient of 0.51 ($p < 0.001$)
 501 (Fig. 11). Multiple linear regression (MLR) models were built to study the linear relationships between PON_{sed} (as the response
 502 variable) and biomass of different types of plankton groups (i.e., PS, PL, and secondary production as explanatory variables).
 503 All variables were normalized within a range from 0 to 1 before model construction. The highest R² was found when PON_{sed}
 504 lagged the explanatory variables by 6 days (Table 4). Regression coefficients were found to be significantly positive between
 505 plankton biomass and PON_{sed}. The contribution of secondary production (coefficient = 0.5388) to PON_{sed} variability was much

506 higher than the contribution from PS (0.4796) or PL (0.4758). Moreover, changes in PS and PL (both normalized) would lead
507 to similar changes in PON_{sed} even though the PL dominated the shelf total production.

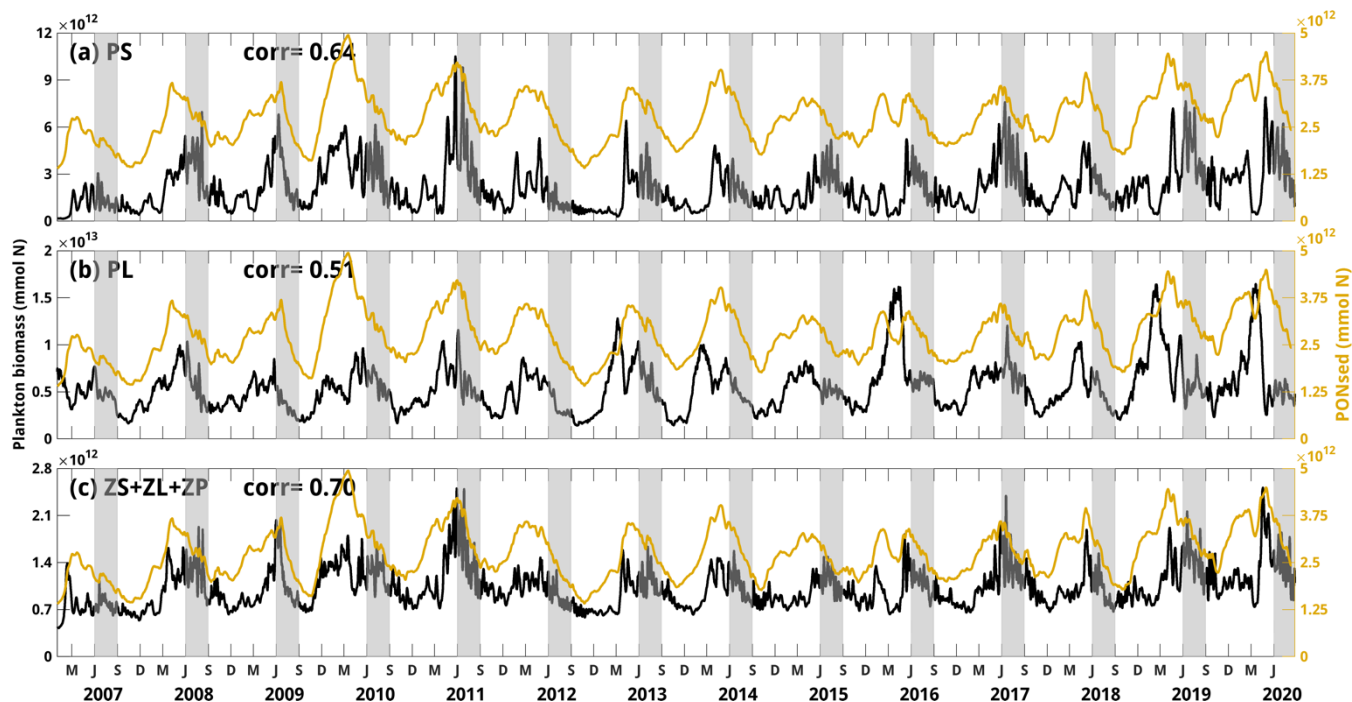
508

509 The results indicate the effects of plankton community structure on PON_{sed} accumulation on the seafloor. A linear function of
510 mortality was applied to PS, PL, ZS, and ZL, while a quadratic mortality function was used for ZP. The modeled mortality
511 rates of PS, PL, ZS, and ZL are thus proportional to the corresponding plankton concentration, the mortality rate at 0 °C, and
512 a temperature-dependent term in which the temperature coefficients were parameterized as 0.0693 °C^{-1} for all groups. The
513 mortality rate of ZP is similar to the other groups but is proportional to the square of ZP concentration. The mortality rates of
514 PS and PL at 0 °C ($Mor_{PS0}=0.002\text{ m}^3\text{ mmol N}^{-1}\text{ day}^{-1}$ and $Mor_{PL0}=0.001\text{ m}^3\text{ mmol N}^{-1}\text{ day}^{-1}$, respectively shown in Table B4)
515 were parameterized 11–22 times lower than those for ZS and ZL ($Mor_{ZS0}=0.022\text{ m}^3\text{ mmol N}^{-1}\text{ day}^{-1}$ and $Mor_{ZL0}=0.022\text{ m}^3$
516 $\text{mmol N}^{-1}\text{ day}^{-1}$) and 60–120 times lower than the parameter for ZP ($Mor_{ZP0}=0.12\text{ m}^3\text{ mmol N}^{-1}\text{ day}^{-1}$). However, concentration
517 (or biomass) ratios between phytoplankton and zooplankton barely reached as high as 10 or more (Fig. 10). Therefore, mortality
518 rates of PS and PL were typically lower than the mortality rates of ZS, ZL, and ZP, given the same ambient water temperature.
519 Through mortality processes, the contribution of zooplankton biomass to water column PON and eventually PON_{sed} was
520 considered greater than that of phytoplankton biomass. In addition, a certain part of zooplankton-induced biomass contributed
521 to the water column PON via egestion processes that were not formulated for the phytoplankton groups. Therefore, the
522 contribution of the secondary production to PON_{sed} exceeded that of the primary production.

523

524 The PS mortality rate was lower than the PL mortality rate as PS concentration was usually less than (non-summer) or nearly
525 (summer) half of the PL concentration. As a result, the variability of PON_{sed} accumulation should be more sensitive to that of
526 PL biomass, which was not supported by the regression model. The top-down effects provide another angle in explaining the
527 regression coefficients. The PS supported the growth of ZS, which was at the bottom trophic level in the zooplankton
528 community. Changes in PS could be reflected in the changes in all types of zooplankton biomass through grazing and predation
529 processes in the zooplankton community (top-down effects as indicated by Fig. 10a and 10c) and further in the changes in
530 PON_{sed} . PL was grazed by ZL and ZP, which were at a higher trophic level than ZS, changes in PL could be mostly reflected
531 in biomass changes in these two groups only. Thus, despite that only half (~51 % on average; figure not shown) of the biomass
532 source in the zooplankton community was supported by PS, a considerable amount of PON_{sed} supported by zooplankton was
533 from PS. This effect offsets the high mortality rate of PL. It may explain the comparable regression coefficients for PS and PL
534 on the PON_{sed} variability.

535



536

537 **Figure 11. Comparisons between daily PON_{sed} and plankton biomass (i.e., (a) PS, (b) PL, and (c) secondary production). All biomass**
 538 **matrices were integrated over the entire water column and the LaTex shelf.**

539

540 **Table 4. A multiple linear regression model with a response variable of PON_{sed} lagging the explanatory variables by 6 days. Note**
 541 **that the model was built upon normalized daily time series.**

Linear regression model:

$$PON_{sed} (\text{lag by 6 days}) \sim 1 + PS + PL + \text{secondary production}$$

Estimated coefficients:

	Estimate	Std. Error	t-statistic	p-value
Intercept	0.0091	0.0036	2.5496	0.01*
PS	0.4796	0.0135	35.5370	<2E-16***
PL	0.4758	0.0084	56.5040	<2E-16***
Secondary production	0.5388	0.0134	40.0680	<2E-16***

Significance codes: 0 (***) 0.001 (**) 0.01 (*)

Number of observations: 4980, Error degrees of freedom: 4976

Root Mean Squared Error: 0.0997

R-squared: 0.74, Adjusted R-Squared: 0.74

542

543 **4.4 Water column DO**

544 In this study, we focus on the responses of bottom DO to the changing nutrient, biomass, and the associated biogeochemical
 545 processes. Thus, it is necessary to compare the contribution of different plankton groups to water DO. Such contributions were
 546 quantified by ratios of total DO generated or consumed by a given plankton group over its biomass. In water above the bottom
 547 2 m, both PS and PL tended to produce more DO than they consumed (Table 5). DO contributed by PS (per mmol N) was at
 548 least twice greater than that by PL. As PL biomass was usually greater than PS biomass (Fig. 10), such differences resulted
 549 from a higher temperature-dependent respiration rate for PL ($K_{ResPL}=0.0693\text{ }^{\circ}\text{C}^{-1}$; Table B4) than for PS ($K_{ResPS}=0.0519\text{ }^{\circ}\text{C}^{-1}$).
 550 DO consumptions by ZS and ZL metabolism were found to be three times greater than those by ZP on average. The rates
 551 of zooplankton metabolism were formulated proportionally to total biomass flows from lower trophic levels. ZS and ZL
 552 consumed more biomass through grazing than ZP, which could be reflected in the percentages of total zooplankton biomass
 553 (ZS accounted for 32 % on average, ZL for 39 %, ZP for 29 %, figure not shown). Taking all plankton functional groups as a
 554 whole, the net DO contribution by the community (per unit biomass) was found to be mostly positive (positive maximum,
 555 median, mean, first quartile, and third quartile; Table 5).

556

557 In the water within the bottom 2 m, the DO consumed by the plankton community had a higher chance to exceed the production
 558 than in the layers above (Table 5). Firstly, the DO production by the phytoplankton community within the bottom 2 m was
 559 found to be nearly half of that found in the layers above, as nutrients and light were more likely to be limited. Secondly, the
 560 first quartile of DO contribution by PL was found to be slightly negative within the bottom 2 m, while in the layers above, the
 561 corresponding statistic was positive. Finally, the net DO contribution was found to be generally positive (mean and median)
 562 but had a higher chance to be negative (minimum and first quartile) than waters above the bottom 2 m. The above statistics
 563 help us to understand how DO changes when nutrient supplies are altered. For example, if riverine nutrient supplies are
 564 reduced, photosynthesis rates will decrease. As the respiration rate of phytoplankton was formulated as a function of water
 565 temperature and phytoplankton concentration only, nutrient changes will not lead to changes in respiration rate per unit
 566 biomass. The net DO production by phytoplankton will decrease.

567

568 **Table 5. Statistics of plankton contribution per unit biomass in producing or consuming DO over water layers above and within the**
 569 **bottom 2 m. Statistics are calculated based on depth-integrated daily matrices without spatial average or spatial integration. Note**
 570 **that negative signs shown denote DO consumption.**

	Contributions at layers above the bottom 2 m (unit: $\times 10^{-5}\text{ }mmol\text{ }O_2\text{ }s^{-1}\text{ }mmol\text{ }N^{-1}$)						
	min	max	median	mean	first quartile	third quartile	Std.
PS	-1.19	27.64	7.45	7.02	3.40	10.42	4.09

PL	-2.10	58.83	2.22	3.03	1.31	3.62	3.40
ZS	0	-23.18	-6.77	-7.25	-3.76	-10.66	4.37
ZL	0	-19.78	-6.42	-6.63	-4.95	-8.10	2.72
ZP	-0.22	-9.60	-2.21	-2.60	-1.64	-3.08	1.42
Entire community	-13.76	35.40	0.99	1.25	0.24	1.94	1.84
Contributions at layers within the bottom 2 m (unit: $\times 10^{-5} \text{ mmol O}_2 \text{ s}^{-1} \text{ mmol N}^{-1}$)							
	min	max	median	mean	first quartile	third quartile	Std.
PS	-1.29	23.69	3.51	3.89	0.21	6.17	4.09
PL	-2.28	46.99	1.38	2.48	-0.40	3.74	4.29
ZS	0	-18.53	-4.17	-4.90	-1.66	-7.11	3.92
ZL	0	-19.00	-5.83	-5.72	-4.50	-7.19	2.50
ZP	0	-9.48	-1.89	-2.01	-1.45	-2.36	1.10
Entire community	-39.77	35.93	0.35	0.33	-1.74	1.75	3.71

571 5 Discussion

572 5.1 Si limitation on PL growth

573 Previous studies suggested that there is potential Si limitation in the LaTex shelf (Quigg et al., 2011; Nelson and Dortch, 1996;
574 Lohrenz et al., 1999) due to the increase in riverine N:Si loads (from 1:3 to 1:1) since the 1950s (Turner et al., 1998). Over the
575 studied period, the ratio of N:Si loads from the Mississippi and Atchafalaya Rivers was slightly greater than 1:1 during late
576 spring and summer, while N:Si over the shelf was usually greater than 2:1 (Fig. 8b). Nelson and Dortch (1996) pointed out
577 that within the plume, > 99 % of silicate supported by rivers was removed by biological uptake during spring and 80–95 %
578 during summer. Cruise observations indicated strong Si limitation over the Mississippi River plume (east of 92°W) during
579 spring and little or no Si limitation during summer (Nelson and Dortch, 1996; Lohrenz et al., 1999). Results of limitation
580 coefficients indicated that Si was more limited than N for the growth of PL during spring and summer (Fig. 9 and C3–C6). It
581 should be noted that the Si limitation was only related to the growth of PL in our model, while the Si limitation found in cruise
582 studies was related to the growth of plankton assemblages. During summer, the biomass of PS and PL reached a similar
583 magnitude showing a shift in phytoplankton composition. As the growth of PS was mostly limited by P during summer,
584 especially over the deep or east shelf, P limitation should be considered equally important as Si limitation on the growth of
585 total phytoplankton. Our model results also suggested that a potential co-limitation of nutrients may be more crucial to shelf
586 productivity than the limitation of a single nutrient type. Indeed, bioassays studies illustrated that co-limitation of N+P or
587 N+P+Si occurred and might have a greater impact on the production than single-nutrient limitation (Zhao and Quigg, 2014;
588 Quigg et al., 2011; Turner and Rabalais, 2013).

590 A critical factor associated with nutrient limitation is the half-saturation coefficient of phytoplankton nutrient uptake. Uptake
 591 kinetic studies for different marine diatom species suggested a wide range of half-saturation coefficients of silicate (
 592 K_{SiOH_4} from 0.85 to 17.4 mmol Si m⁻³; Table 6). The average, median, first quartile, and third quartile of the listed measured
 593 coefficients in Table 6 were found to be 5.9, 4.5, 2.3, and 7.0 mmol Si m⁻³, respectively. In our model, the half-saturation
 594 coefficient of silicate uptake by PL was then set as 6.0 mmol Si m⁻³. We applied the average rather than the median of the
 595 published coefficients to our model since the PL group should be considered as a marine diatom assemblage. However, the
 596 K_{SiOH_4} for a diatom assemblage may shift given changing ambient silicate concentration. For example, as pointed out by
 597 Nelson and Dortch (1996), K_{SiOH_4} for the sampled phytoplankton assemblage (dominated by diatom species) remained low
 598 from 0.48 to 1.71 mmol Si m⁻³ when the ambient silicate concentration was low between 0.13 to 0.41 mmol Si m⁻³, but increased
 599 to 5.29 mmol Si m⁻³ as ambient silicate concentration was 4.72 mmol Si m⁻³. Further investigations and improvements in model
 600 parameterization for the dependency of K_{SiOH_4} on silicate concentration are therefore needed.

601

602 **Table 6. Half-saturation coefficient (unit: mmol Si m⁻³) for silicate uptake by different diatom species according to multiple uptake**
 603 **kinetic studies.**

Diatom species	K_{SiOH_4}	Reference
<i>Cylindrotheca fusiformis</i>	0.85	Del Amo and Brzezinski (1999)
<i>Nitzschia alba</i>	6.8	Azam (1974)
<i>Nitzschia alba</i>	4.5	Azam et al. (1974)
<i>Phaeodactylum tricornutum</i>	4.0, 9.2, 6.3	Del Amo and Brzezinski (1999)
<i>Thalassiosira nordenskiöldii</i>	2.8	Kristiansen and Hoell, (2002)
<i>Thalassiosira pseudonana</i>	7.04	Thamatrakoln and Hildebrand (2008)
<i>Thalassiosira pseudonana</i>	1.4	Del Amo and Brzezinski (1999)
<i>Thalassiosira pseudonana</i>	0.8, 2.3	Nelson et al. (1976)
<i>Thalassiosira weissflogii</i>	15.2, 17.4	Milligan et al. (2004)
<i>Thalassiosira weissflogii</i>	4.5	Del Amo and Brzezinski (1999)
Average	5.9	
Diatom functional group (PL)	6.0	This study

604 5.2 Riverine nutrient reductions

605 Since 2001, the Mississippi River/Gulf of Mexico Hypoxia Task Force has set up a goal of controlling the size of the mid-
 606 summer hypoxic zone below 5000 km² in a 5-year running average (Mississippi River/Gulf of Mexico Watershed Nutrient
 607 Task Force, 2001; 2008) by reducing riverine nutrient loads. Fennel and Laurent (2018) suggested that a reduction of 63 ±

608 18% (referred to as the 2000–2016 average) in total N loads or a dual reduction of $48 \pm 21\%$ in total N and P loads could be
 609 necessary to fulfill the hypoxia reduction goal. Statistic models (Scavia et al., 2013; Obenour et al., 2015; Turner et al., 2012;
 610 Laurent and Fennel, 2019) suggested a nutrient reduction of 52%–58% related to the 1980–1996 average should be enough to
 611 fulfill the goal. Nonetheless, inorganic nutrient types considered in these statistical models were either N-based (i.e., ammonia
 612 and nitrite+nitrate) or a combination of N and P-based nutrients. The plankton community embedded in existing models was
 613 simplified with one phytoplankton functional group and one zooplankton functional group (e.g., Fennel et al., 2006, 2011,
 614 2013; Fennel and Laurent, 2018; Justić and Wang, 2014). Here we aimed to explore the sensitivity of bottom DO to the riverine
 615 nutrient discharge with different nutrient (N, P, and Si) reduction combinations, the corresponding changes in plankton
 616 community, and implications for hypoxia reduction. A total of six sensitivity experiments (Table 7) were set up with different
 617 combinations of nutrient reductions. The riverine nutrient concentration was the only variable adjusted among these sensitivity
 618 tests. To remove numerical bias introduced by initial conditions, all sensitivity experiments were initialized on 1 January 2012
 619 based on the output of the long-term simulations and were conducted from 1 January 2012 to 26 August 2020. Thus, any
 620 changes in bottom DO due to nutrient reductions should result from changes in biogeochemical processes, including changes
 621 in SOC, changes in DO at the water within the bottom 2 m, and changes in DO at layers above the bottom 2 m.
 622

623 **Table 7. Riverine inorganic nutrient reduction percentages for different sensitivity experiments. Note that all the runs listed were**
 624 **initialized on 1 January 2012 and were conducted from 1 January 2012 to 26 August 2020.**

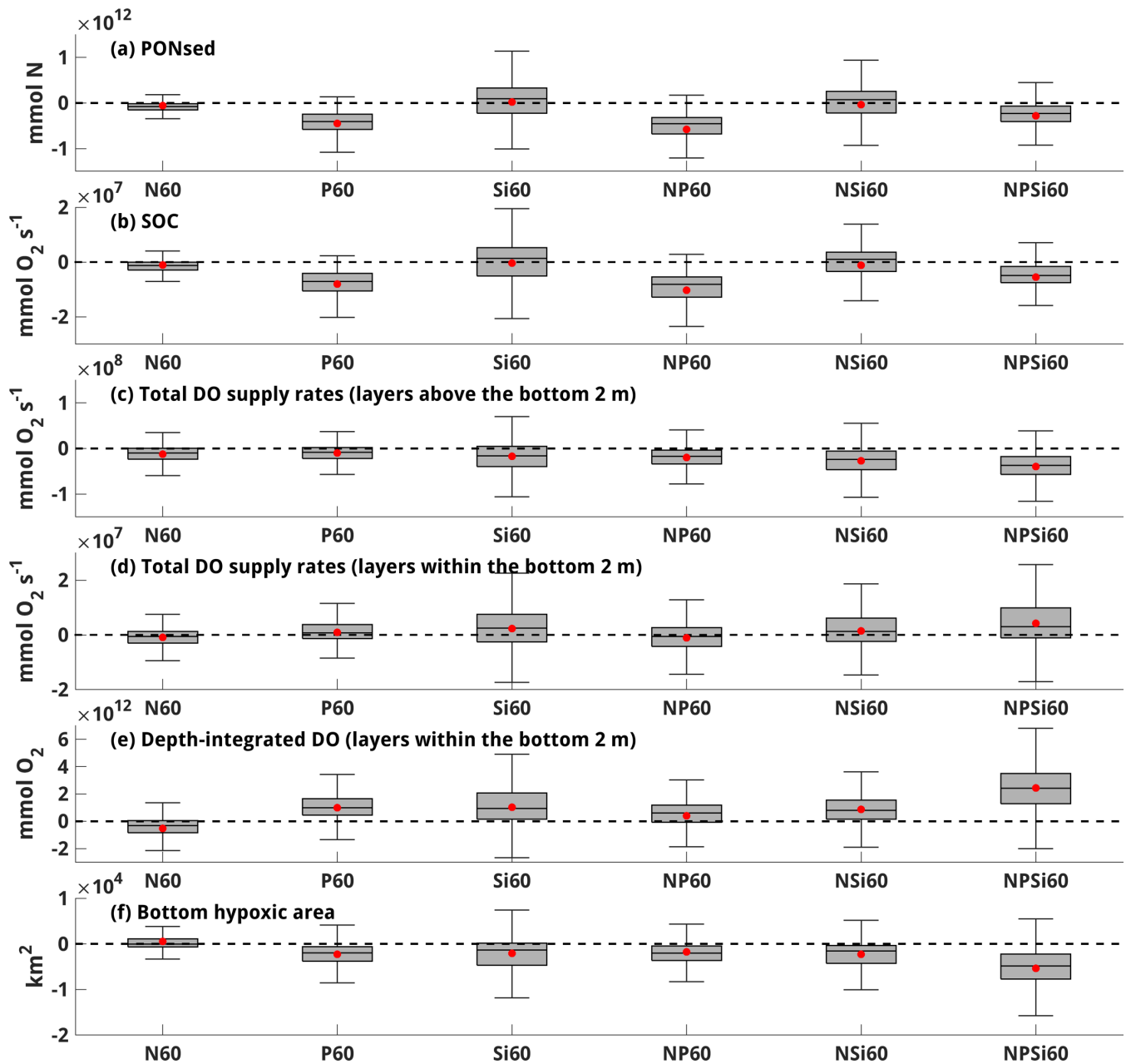
Experiment	Riverine inorganic nutrients reduction percentages (%)		
	N	P	Si
control	0	0	0
N60	60	0	0
P60	0	60	0
Si60	0	0	60
NP60	60	60	0
NSi60	60	0	60
NPSi60	60	60	60

625

626 5.2.1 Responses of PON_{sed} and SOC

627 The total biomass of PON_{sed} was likely to decrease in all nutrient reduction scenarios except for experiments Si60 and NSi60
 628 (Fig. 12a). Responses in SOC (Fig. 12b) followed strictly with those in PON_{sed} , as SOC was formulated as a function of PON_{sed}
 629 and water temperature and the latter remained unchanged among the six experiments. We found different responses in PON_{sed}
 630 (or SOC) in different nutrient reduction strategies. The changes in depth-integrated plankton biomass over the entire column
 631 can help to explain such differences (Fig. C7). As discussed above, the variability of PON_{sed} was mainly from that of secondary
 632 production (Fig. 11 and Table 4). In most of the sensitivity tests (N60, P60, NP60, and NPSi60), the secondary production

633 experienced a salient decrease (Fig. C7b) due to fewer food supply (Fig. C7c). PON_{sed} or SOC, therefore, decreased in these
634 scenarios. However, in scenarios Si60 and NSi60, secondary production did not exhibit pronounced changes (near-zero mean
635 and median; Fig C7b) but either increased or decreased in nearly half of the simulation. Such a high uncertainty could lead to
636 either an increase or a decrease in PON_{sed} biomass (Fig. 12a). On average, a slightly positive change in PON_{sed} biomass was
637 simulated, which should be a result of an enlarging ZS group (Fig. C7d) and can be explained by bottom-up and top-down
638 effects. As the growth of PL was commonly limited by Si on the shelf (Fig. 9 and C3–C6), PL biomass would generally
639 decrease (Fig. C7g) as Si loads were reduced. It would further lead to biomass decreases in ZL (Fig. C7f) and ZP (Fig. C7h),
640 both of which grazed on PL (bottom-up effects). ZS biomass would likely increase (top-down; Fig. C7d) as the predation
641 pressure from ZL and ZP was weakened. Such responses in scenarios Si60 and NSi60 can also be found for the biomass
642 integrated over the layers above the bottom 2 m (Fig. C8).



644

645 Figure 12. Responses of (a) PON_{sed} , (b) SOC, (c) total DO supply rates in layers above the bottom 2 m, (d) total DO supply rates at
 646 layers within the bottom 2 m, (e) depth-integrated DO over layers within the bottom 2 m, and (f) bottom hypoxic area. Note that
 647 total DO supply rates in (c–d) are the results of photosynthesis rates minus total water column respiration rates. Statistics shown
 648 are mean (red dots), median, first quartile, third quartile, minimum, and maximum derived from the differences between sensitivity
 649 tests and the control run during late spring and summer (May–August). A positive (negative) value indicates an increasing
 650 (decreasing) DO consumption rate by SOC in (b) but represents an increasing (decreasing) DO supply rate by water column
 651 biogeochemical processes in (c–d).

652 5.2.2 Responses of DO in water columns

653 Among the six experiments, responses in biomass regarding reduced river nutrient loads are similar at the layers above the
654 bottom 2 m (Fig. C8) and over the entire column (Fig. C7). Changes in total DO supply rates (Fig. 12c) and total production
655 (Fig. C8a) generally exhibited a negative pattern in all nutrient reduction scenarios. Such responses are expected in the upper
656 water column as the plankton community produced more DO than it consumed (Table 5) even though when nutrient supplies
657 were reduced. Decreases in total production would lead to decreases in DO supplies. The most significant decreases in total
658 biomass and DO supplies occurred when N, P, and Si loads were all reduced by 60 % (NPSi60), while minor decreases occurred
659 in experiment N60. Our simulations suggested that the primary production on the shelf was more limited by P and Si rather
660 than by N only. Therefore, the changes in biomass would be less pronounced in N60 than in other scenarios.

661

662 Response in total DO supplies to nutrient reductions became more complicated when reaching down near the bottom, where
663 net DO contribution from the community (i.e., (photosynthesis - total respiration)/total biomass) would be more likely to shift
664 between positive and negative than in the upper water column (Table 5). But detailed responses varied from case to case. In
665 scenario N60, most of the time, the plankton community produced more DO than it consumed in water within the bottom 2 m
666 (same as in the control experiment), as decreases in N may not lead to a dramatic decrease in photosynthesis rate. Decreases
667 in total production (Fig. C9a) would result in lower DO production rates (negative mean and median of changes in total DO
668 supply rates for N60 shown in Fig. 12d). However, net DO contributions from plankton community can switch to negative
669 when N limitation was commonly detected (e.g., 2012, 2014, and 2018, Fig. 9). The photosynthesis rates can be significantly
670 restricted below the total respiration rates, indicating that decreases in total production would lead to less DO consumption or
671 increase in net DO supply rates (positive interval in Fig. 12d for N60).

672

673 In scenarios P60, Si60, NSi60, and NPSi60, changes in total biomass (negative; Fig. C9a) and total DO supply rates (positive;
674 Fig. 12d) were in opposite phases, suggesting that net DO contribution by the community was usually negative at layers within
675 the bottom 2 m. The shifts in net DO contribution in these cases mainly result from the reductions in limited nutrients (i.e., P
676 and Si). Photosynthesis rates decrease pronouncedly below the total respiration rates, leading to a negative net DO contribution.
677 A great uncertainty in changes in total DO supply rates (wide range of quartiles; Fig. 12d) was found when P load reduction
678 was not incorporated (i.e., Si60 and NSi60). It can be explained by different responses of biomass in the plankton community
679 due to competition, bottom-up effects, and top-down effects. Reductions in Si supplies would lead to less PL (Fig. C9g) but
680 more PS (Fig. C9e) and introduce more uncertainty in primary production (Fig., C9c). Unlike at the layers above, here, near
681 the bottom, increases in ZS (Fig. C9d) might be more related to bottom-up effects rather than top-down effects as ZL and ZP
682 did not exhibit pronounced changes (Fig. C9f and C9h). Such responses in ZL and ZP were a combined effect of increased
683 food supply from PS but less from PL. Thus, high uncertainty in responses in the secondary productions was also found (Fig.
684 C9b). In scenario NP60, within the bottom 2 m, total plankton biomass experienced a salient decrease (Fig. C9a), while changes

685 in total DO supply rates fluctuated around zero with a slightly negative mean and median (Fig. 12d). It indicated that net DO
686 contribution by the plankton community shifted between positive and negative in this experiment. Such complex responses in
687 the biomass and in the plankton community's role in DO contribution highlight the need for a multi-group plankton
688 parameterization in hypoxia simulation.

689 **5.2.3 Responses in bottom DO and hypoxic area**

690 The responses in bottom DO and hypoxic area to nutrient reductions are a combined effect of changes of DO in sediment and
691 water column. The most significant decrease in SOC (Fig. 12b) may not necessarily lead to the most significant increase
692 (decrease) in bottom DO (hypoxic area) (e.g., NP60; Fig. 12e–12f), while the most significant drop in DO supplies in the upper
693 layers (Fig. 12c) may not cause a pronounced decrease in bottom DO (e.g., NPSi60; Fig. 12e–12f). The most significant
694 increase in bottom DO was found when supplies of all three types of nutrients were reduced by 60 % (NPSi60), where the
695 bottom hypoxic area (2012-2000) reached 5275 km². The size of the hypoxic area was also saliently reduced in P60, Si60,
696 NP60, and NSi60. For NPSi60 and P60, SOC rates dropped saliently (Fig. 12b), corresponding with an increase in total DO
697 supply rates by water column biogeochemical processes at layers within the bottom 2 m (Fig. 12d). Although DO supplies
698 from the upper layers decreased in these two scenarios, bottom hypoxia would still be significantly relieved. In scenarios of
699 Si60, NP60, and NSi60, a more significant uncertainty was found in the responses of bottom DO and hypoxic area (Fig. 12e–
700 12f), which could be attributed to the different responses of the five plankton groups (Fig. C7 and C9).

701

702 Intriguingly, compared to existing models (e.g., Justić et al., 2003, 2007; Laurent and Fennel, 2014; Fennel and Laurent, 2018)
703 or statistical studies (Scavia et al., 2013; Obenour et al., 2015; Turner et al., 2012; Laurent and Fennel, 2019), our model
704 simulated a different response of hypoxia development when only N is reduced by 60% (N60 Fig. 12e–12f). Existing studies
705 generally agree that a 60% reduction in N load will reduce SOC and thus relieve the hypoxic condition. In this study, For N60,
706 as fewer productions are supported, we found the magnitude of DO reduction (less production) in the water column (both
707 upper and bottom layers) exceeded that of SOC reduction (less consumption), resulting in a decrease in bottom DO and worsen
708 the hypoxic condition.

709 **5 Conclusions**

710 We modified a three-dimensional coupled hydrodynamic–biogeochemical model (NEMURO) and adapted it to the Gulf of
711 Mexico to study the bottom DO variability in the LaTex Shelf. In addition to N and Si, a P flow was embedded into the
712 NEMURO model to account for the impacts of P limitation on hypoxia development. Built on the SOC scheme of the
713 instantaneous remineralization developed by Fennel et al. (2006), a pool of sedimentary PON was added to account for
714 temporal delays in SOC to the peak of plankton blooms. The model can well reproduce the vertical profiles of inorganic
715 nutrient concentration (i.e., nitrate, phosphate, and silicate), the ratio of diatom/total phytoplankton, and the magnitude of SOC.

716 The model's robustness in DO simulation was affirmed via 1) comparison of the DO profiles against cruise observations from
717 two different databases, 2) comparison of spatial distributions of bottom DO, and 3) time series of the hypoxic area against the
718 shelf-wide cruise observations.

719

720 Model results suggested that P and Si limitations could be more common than previously reported. N limitation was more
721 commonly found in the shallow (< 20 m) middle and west shelf for both PS and PL, while in the other parts, primary production
722 was more likely to be limited by P or Si. PL was found as a dominant plankton group accounting for about 50 – 70 % of total
723 production during early spring and summer, explaining 63 % of the daily variability of the total production. The contribution
724 of PS supported about 20 – 35 % of total biomass. The seasonality of total production exhibited a bi-peak (in late spring and
725 early summer) pattern, which can be explained by the competition between PS and PL and was hardly captured by previous
726 numerical models. We further explored the plankton contribution to DO budgets in water and sediment layers, respectively.
727 We found 1) the PON_{sed} pool was contributed mainly by zooplankton mortality and egestion, 2) the plankton community, in
728 general, produced more DO than it consumed in the waters above the bottom 2 m, with more uncertainty within the bottom 2
729 m of waters.

730

731 The types of limited nutrients, interactions (competition, grazing, and predation behaviors) among plankton groups, and the
732 shifts in net DO contribution by the plankton community lead to complex responses in biomass, water DO, and bottom hypoxia.
733 A 60 % reduction in all nutrient supplies would achieve the hypoxic area reduction goal set by the Task Force. The complex
734 responses in the plankton biomass and their contribution to DO variation highlighted the importance of the complexity of the
735 plankton community in the hypoxia evolution.

736

737 **Code/Data availability:** Model data is available at the LSU mass storage system and details are on the webpage of the Coupled
738 Ocean Modeling Group at LSU (<https://faculty.lsu.edu/zxue/>). Data requests can be sent to the corresponding author via this
739 webpage.

740

741 **Author contribution:** Z. George Xue designed the experiments and Yanda Ou carried them out. Yanda Ou developed the
742 model code and performed the simulations. Yanda Ou and Z. George Xue prepared the manuscript.

743

744 **Competing interests:** The authors declare that they have no conflict of interest.

745

746 **Acknowledgment:** Research support was provided through the Bureau of Ocean Energy Management (M17AC00019,
747 M20AC10001). We thank Dr. Jerome Fiechter at UC Santa Cruz for sharing his NEMURO model codes and Dr. Katja Fennel
748 at Dalhousie University for discussing model parameterization. The computational resource was provided by the High-
749 Performance Computing Facility (clusters SuperMIC and QueenBee3) at Louisiana State University.

750
751

752 **Appendix A: Expressions of processes terms modified in this study**

753 Detailed descriptions of related terms and parameters are listed in Appendix B.

754 **A1 Update gross primary production of PS and PL due to the additional phosphate limitation**

755 $GppPSn = GppNPS + GppAPS,$ (A1)

756 $GppPLn = GppNPL + GppAPL,$ (A2)

757 where,

758 $GppNPS = PSn V_{maxS} \exp(K_{GppS} TMP) \left[1 - \exp\left(-\frac{\alpha_{PS}}{V_{maxS}} I_{PS}\right)\right] \exp\left(-\frac{\beta_{PS}}{V_{maxS}} I_{PS}\right) NutlimPS RnewS,$ (A3)

759 $GppAPS = PSn V_{maxS} \exp(K_{GppS} TMP) \left[1 - \exp\left(-\frac{\alpha_{PS}}{V_{maxS}} I_{PS}\right)\right] \exp\left(-\frac{\beta_{PS}}{V_{maxS}} I_{PS}\right) NutlimPS (1 - RnewS),$ (A4)

760 $GppNPL = PLn V_{maxL} \exp(K_{GppL} TMP) \left[1 - \exp\left(-\frac{\alpha_{PL}}{V_{maxL}} I_{PL}\right)\right] \exp\left(-\frac{\beta_{PL}}{V_{maxL}} I_{PL}\right) NutlimPL RnewL,$ (A5)

761 $GppAPL = PLn V_{maxL} \exp(K_{GppL} TMP) \left[1 - \exp\left(-\frac{\alpha_{PL}}{V_{maxL}} I_{PL}\right)\right] \exp\left(-\frac{\beta_{PL}}{V_{maxL}} I_{PL}\right) NutlimPL (1 - RnewL),$ (A6)

762

763 $RnewS = \frac{NO_3}{(NO_3 + K_{NO_3S}) \left(1 + \frac{NH_4}{K_{NH_4S}}\right)} \frac{1}{\frac{NO_3}{(NO_3 + K_{NO_3S}) \left(1 + \frac{NH_4}{K_{NH_4S}}\right)} + \frac{NH_4}{NH_4 + K_{NH_4S}}},$ (A7)

764 $RnewL = \frac{NO_3}{(NO_3 + K_{NO_3L}) \left(1 + \frac{NH_4}{K_{NH_4L}}\right)} \frac{1}{\frac{NO_3}{(NO_3 + K_{NO_3L}) \left(1 + \frac{NH_4}{K_{NH_4L}}\right)} + \frac{NH_4}{NH_4 + K_{NH_4L}}},$ (A8)

765 $NutlimPS = \min\left(\frac{NO_3}{(NO_3 + K_{NO_3S}) \left(1 + \frac{NH_4}{K_{NH_4S}}\right)} + \frac{NH_4}{NH_4 + K_{NH_4S}}, \frac{PO_4}{PO_4 + K_{PO_4S}}\right),$ (A9)

766 $NutlimPL = \min\left(\frac{NO_3}{(NO_3 + K_{NO_3L}) \left(1 + \frac{NH_4}{K_{NH_4L}}\right)} + \frac{NH_4}{NH_4 + K_{NH_4L}}, \frac{PO_4}{PO_4 + K_{PO_4L}}, \frac{SiOH_4}{SiOH_4 + K_{SiOH_4L}}\right),$ (A10)

767 $I_{PS} = PAR \text{ frac} \exp\left\{z \text{ AttSW} + \text{AttPS} \int_z^0 [PSn(\zeta) + PLn(\zeta)] d\zeta\right\},$ (A11)

768 $I_{PL} = PAR \text{ frac} \exp\left\{z \text{ AttSW} + \text{AttPL} \int_z^0 [PSn(\zeta) + PLn(\zeta)] d\zeta\right\},$ (A12)

769 **A2 Update aerobic decomposition from PON to NH₄ and from DON to NH₄ due to the introduction of oxygen dependency**
770

771 $DecP2N = PON VP2N_0 \exp(K_{P2N} TMP) \hat{r},$ (A13)

772 $DecD2N = PON VD2N_0 \exp(K_{D2N} TMP) \hat{r},$ (A14)

773 where,

774 $\hat{r} = \max\left[\frac{\max(0, O_{xyg} - O_{xyg_{th}})}{K_{O_{xyg}} + O_{xyg} - O_{xyg_{th}}}, 0\right],$ (A15)

775 **A3 Update water column nitrification due to the introduction of oxygen dependency and light limitation**

776 $Nit = Nit_0 \exp(K_{Nit} TMP) LgtlimN \hat{r}$, (A16)

777 where,

778 $LgtlimN = 1 - \max\left(0, \frac{I_N - I_0}{I_N - I_0 + k_I}\right)$, (A17)

779 $I_N = PAR \text{ frac} \exp\left\{z \text{ AttSW} + \max(\text{AttPS}, \text{AttPL}) \int_z^0 [PSn(\zeta) + PLn(\zeta)] d\zeta\right\}$, (A18)

780 **A4 Additional SOC term:**

781 $SOC = 8.3865 PON_{sed} VP2N_0 \exp(K_{P2N} TMP)$, (A19)

782 **Appendix B: Descriptions of terms and parameters**

783 **Table B1. Descriptions of state variables**

Terms	Description	Unit
NH_4	Ammonium concentration	mmolN m ⁻³
NO_3	Nitrate concentration	mmolN m ⁻³
PO_4	Phosphate concentration	mmolP m ⁻³
DOP	Dissolved organic phosphorus concentration	mmolP m ⁻³
POP	Particulate organic phosphorus concentration	mmolP m ⁻³
$SiOH_4$	Silicate concentration	mmolSi m ⁻³
PSn	Small phytoplankton biomass concentration measured in nitrogen	mmolN m ⁻³
PLn	Large phytoplankton biomass concentration measured in nitrogen	mmolN m ⁻³
$Oxyg$	Dissolved oxygen concentration	mmolO ₂ m ⁻³

784

785 **Table B2 Descriptions of related terms involved in the phosphorus cycle and nutrient limitation. Superscripts “*” and “+” denote**
 786 **that the mathematic expressions of corresponding terms are the same as those in Kishi et al. (2007) and Shropshire et al. (2020),**
 787 **respectively. Expressions of terms with no superscript are updated and reported in Appendix A.**

Terms	Description	Unit
$DecP2N$	Decomposition rate from PON to NH ₄	mmolN m ⁻³ day ⁻¹
$DecD2N$	Decomposition rate from DON to NH ₄	mmolN m ⁻³ day ⁻¹
$DecP2D^{*+}$	Decomposition rate from PON to DON	mmolN m ⁻³ day ⁻¹
$EgeZLn^+$	Large zooplankton egestion rate measured in nitrogen	mmolN m ⁻³ day ⁻¹
$EgeZPn^{*+}$	Predatory zooplankton egestion rate measured in nitrogen	mmolN m ⁻³ day ⁻¹

<i>EgeZSn</i> ^{*+}	Small zooplankton egestion rate measured in nitrogen	mmolN m ⁻³ day ⁻¹
<i>ExcPSn</i> ^{*+}	Small phytoplankton extracellular excretion rate to DON and is measured in nitrogen	mmolN m ⁻³ day ⁻¹
<i>ExcPLn</i> ^{*+}	Large phytoplankton extracellular excretion rate to DON and is measured in nitrogen	mmolN m ⁻³ day ⁻¹
<i>ExcZSn</i> ^{*+}	Small zooplankton excretion rate to NH ₄ and is measured in nitrogen	mmolN m ⁻³ day ⁻¹
<i>ExcZLn</i> ⁺	Large zooplankton excretion rate to NH ₄ and is measured in nitrogen	mmolN m ⁻³ day ⁻¹
<i>ExcZPn</i> ^{*+}	Predatory zooplankton excretion rate to NH ₄ and is measured in nitrogen	mmolN m ⁻³ day ⁻¹
<i>GppNPS</i>	Small phytoplankton nitrate-induced gross primary production rate measured in nitrogen	mmolN m ⁻³ day ⁻¹
<i>GppAPS</i>	Small phytoplankton ammonium-induced gross primary production rate measured in nitrogen	mmolN m ⁻³ day ⁻¹
<i>GppPSn</i>	Small phytoplankton gross primary production rate measured in nitrogen	mmolN m ⁻³ day ⁻¹
<i>GppNPL</i>	Large phytoplankton nitrate-induced gross primary production rate measured in nitrogen	mmolN m ⁻³ day ⁻¹
<i>GppAPL</i>	Large phytoplankton ammonium-induced gross primary production rate measured in nitrogen	mmolN m ⁻³ day ⁻¹
<i>GppPLn</i>	Large phytoplankton gross primary production rate measured in nitrogen	mmolN m ⁻³ day ⁻¹
<i>MorPSn</i> ⁺	Small phytoplankton mortality rate measured in nitrogen	mmolN m ⁻³ day ⁻¹
<i>MorPLn</i> ⁺	Large phytoplankton mortality rate measured in nitrogen	mmolN m ⁻³ day ⁻¹
<i>MorZSn</i> ⁺	Small zooplankton mortality rate measured in nitrogen	mmolN m ⁻³ day ⁻¹
<i>MorZLn</i> ⁺	Large zooplankton mortality rate measured in nitrogen	mmolN m ⁻³ day ⁻¹
<i>MorZPn</i> ^{*+}	Predatory zooplankton mortality rate measured in nitrogen	mmolN m ⁻³ day ⁻¹
<i>Nit</i>	Nitrification rate	mmolN m ⁻³ day ⁻¹
<i>ResPSn</i> ^{*+}	Small phytoplankton respiration rate measured in nitrogen	mmolN m ⁻³ day ⁻¹
<i>ResPLn</i> ^{*+}	Large phytoplankton respiration rate measured in nitrogen	mmolN m ⁻³ day ⁻¹
<i>SOC</i>	Sediment oxygen consumption rate	mmolO ₂ m ⁻² day ⁻¹

788

789 **Table B3 Descriptions of other variables**

Terms	Description	Unit
I_{PS}	Photosynthetically available radiation for small phytoplankton	$W m^{-2}$
I_{PL}	Photosynthetically available radiation for large phytoplankton	$W m^{-2}$
I_N	Maximum photosynthetically available radiation	$W m^{-2}$
$LgtlimN$	Light inhibition on nitrification rate	no dimension
$NutlimPS$	Nutrient limitation term for small phytoplankton	no dimension
$NutlimPL$	Nutrient limitation term for large phytoplankton	no dimension
PAR	Net short-wave radiation on water surface	$W m^{-2}$
\hat{f}	Oxygen inhibition on nitrification and aerobic decomposition rates	no dimension
$RnewS$	The f-ratio of small phytoplankton which is defined by the ratio of nitrate uptake to total uptake of nitrate and ammonium	no dimension
$RnewL$	The f-ratio of large phytoplankton which is defined by the ratio of nitrate uptake to total uptake of nitrate and ammonium	no dimension
$Thickness_{bot}$	Thickness of the bottom water layer	m
TMP	Water temperature	$^{\circ}C$
z, ζ	Vertical coordinate which is negative below sea surface	m

790

791 **Table B4. Descriptions and values of all model parameters. Superscripts “S”, “L”, “F06”, and “F13” denote that the corresponding**
792 **parameters follow Shropshire et al. (2020), Laurent et al. (2012), Fennel et al. (2006), and Fennel et al. (2013), respectively.**
793 **Superscript “*” indicates the corresponding parameters are from this study.**

Parameter	Description	Units	Values
Small phytoplankton			
V_{maxS}	Small phytoplankton maximum photosynthetic rate at 0 $^{\circ}C$	day^{-1}	0.4 ^S
K_{NO_3S}	Small Phytoplankton half saturation constant for nitrate	$mmolN m^{-3}$	0.5 ^S
K_{NH_4S}	Small Phytoplankton half saturation constant for ammonium	$mmolN m^{-3}$	0.1 ^S
K_{PO_4S}	Small Phytoplankton half saturation constant for phosphate	$mmolP m^{-3}$	0.5 ^L
α_{PS}	Small phytoplankton photochemical reaction coefficient, initial slope of P-I curve	$m^2 W^{-1} day^{-1}$	0.1 ^S

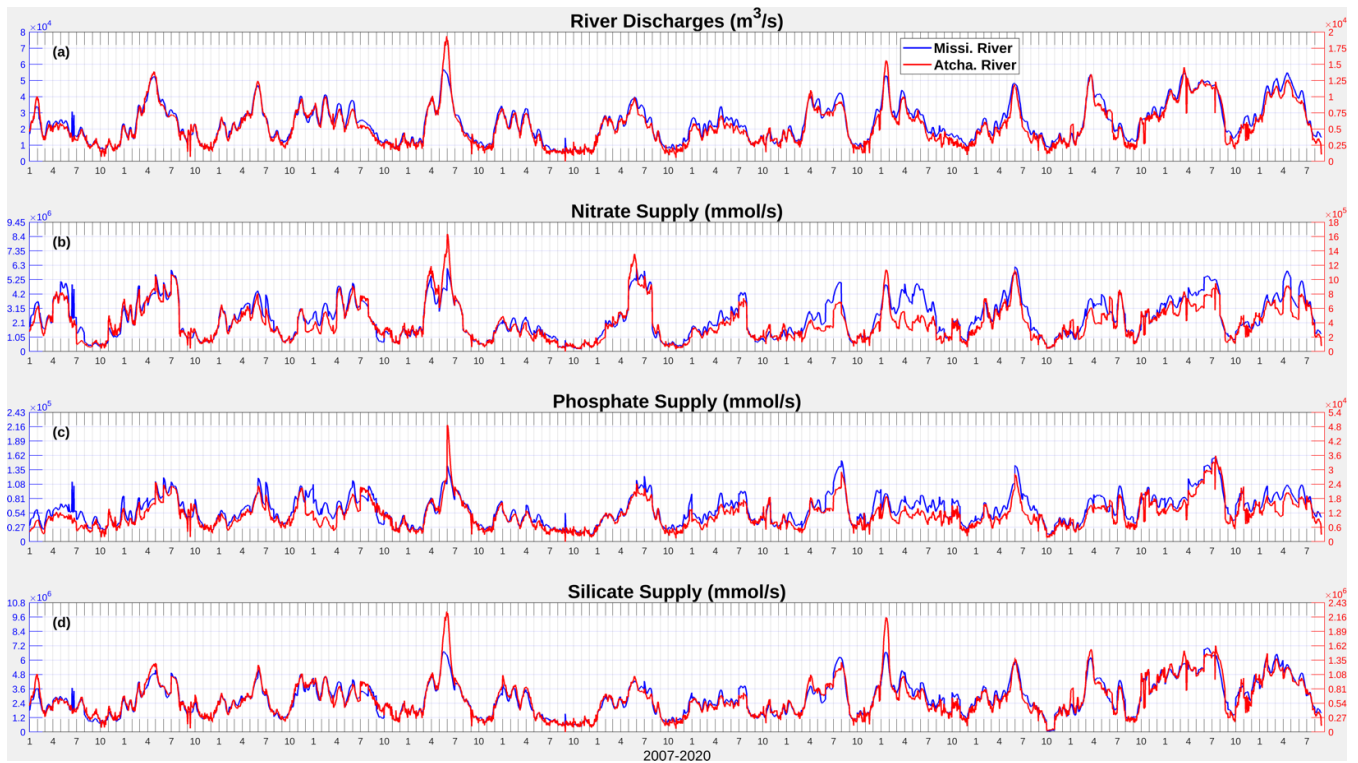
β_{PS}	Small phytoplankton photoinhibition coefficient	$\text{m}^2 \text{W}^{-1} \text{day}^{-1}$	0.00045 ^S
Res_{PS0}	Small phytoplankton respiration rate at 0 °C	day^{-1}	0.03 ^S
Mor_{PS0}	Small phytoplankton mortality rate at 0 °C	$\text{m}^3 \text{mmolN}^{-1} \text{day}^{-1}$	0.002 ^S
γ_S	Ratio of extracellular excretion to photosynthesis for small phytoplankton	no dimension	0.135 ^S
K_{GPPS}	Small phytoplankton temperature coefficient for photosynthetic rate	$^{\circ}\text{C}^{-1}$	0.0693 ^S
K_{ResPS}	Small phytoplankton temperature coefficient for respiration	$^{\circ}\text{C}^{-1}$	0.0519 ^S
K_{MorPS}	Small phytoplankton temperature coefficient for mortality	$^{\circ}\text{C}^{-1}$	0.0693 ^S
Large phytoplankton			
V_{maxL}	Large phytoplankton maximum photosynthetic rate at 0 °C	day^{-1}	0.8 ^S
K_{NO_3L}	Large Phytoplankton half saturation constant for nitrate	mmolN m^{-3}	3.0 ^S
K_{NH_4L}	Large Phytoplankton half saturation constant for ammonium	mmolN m^{-3}	0.3 ^S
K_{PO_4L}	Large Phytoplankton half saturation constant for phosphate	mmolP m^{-3}	0.5 ^L
K_{SiOH_4L}	Large Phytoplankton half saturation constant for silicate	mmolSi m^{-3}	6.0 ^S
α_{PL}	Large phytoplankton photochemical reaction coefficient, initial slope of P-I curve	$\text{m}^2 \text{W}^{-1} \text{day}^{-1}$	0.1 ^S
β_{PL}	Large phytoplankton photoinhibition coefficient	$\text{m}^2 \text{W}^{-1} \text{day}^{-1}$	0.00045 ^S
Res_{PL0}	Large phytoplankton respiration rate at 0 °C	day^{-1}	0.03 ^S
Mor_{PL0}	Large phytoplankton mortality rate at 0 °C	$\text{m}^3 \text{mmolN}^{-1} \text{day}^{-1}$	0.001 ^S

γ_L	Ratio of extracellular excretion to photosynthesis for large phytoplankton	no dimension	0.135 ^S
K_{GppL}	Large phytoplankton temperature coefficient for photosynthetic rate	$^{\circ}\text{C}^{-1}$	0.0693 ^S
K_{MorPL}	Large phytoplankton temperature coefficient for mortality	$^{\circ}\text{C}^{-1}$	0.0693 ^S
K_{ResPL}	Large phytoplankton temperature coefficient for respiration	$^{\circ}\text{C}^{-1}$	0.0693 ^S
Small zooplankton			
GR_{maxSps}	Small zooplankton maximum grazing rate on small phytoplankton at 0 $^{\circ}\text{C}$	day^{-1}	0.6 ^S
λ_S	Ivlev constant of small zooplankton	$\text{m}^3 \text{mmolN}^{-1}$	1.4 ^S
$PS2ZS$	Small zooplankton threshold value for grazing on small phytoplankton	mmolN m^{-3}	0.043 ^S
α_{ZS}	Assimilation efficiency of small zooplankton	no dimension	0.7 ^S
β_{ZS}	Growth efficiency of small zooplankton	no dimension	0.3 ^S
Mor_{ZS0}	Small zooplankton mortality rate at 0 $^{\circ}\text{C}$	$\text{m}^3 \text{mmolN}^{-1} \text{day}^{-1}$	0.022 ^S
K_{GraS}	Small zooplankton temperature coefficient for grazing	$^{\circ}\text{C}^{-1}$	0.0693 ^S
K_{MorZS}	Small zooplankton temperature coefficient for mortality	$^{\circ}\text{C}^{-1}$	0.0693 ^S
Large zooplankton			
GR_{maxLps}	Large zooplankton maximum grazing rate on small phytoplankton at 0 $^{\circ}\text{C}$	day^{-1}	0 ^S
GR_{maxLpl}	Large zooplankton maximum grazing rate on large phytoplankton at 0 $^{\circ}\text{C}$	day^{-1}	0.3 ^S
GR_{maxLzs}	Large zooplankton maximum grazing rate on small zooplankton at 0 $^{\circ}\text{C}$	day^{-1}	0.3 ^S
λ_L	Ivlev constant of large zooplankton	$\text{m}^3 \text{mmolN}^{-1}$	1.4 ^S
$PL2ZL$	Large zooplankton threshold value for grazing on large phytoplankton	mmolN m^{-3}	0.040 ^S

<i>ZS2ZL</i>	Large zooplankton threshold value for grazing on small zooplankton	mmolN m^{-3}	0.040 ^S
α_{ZL}	Assimilation efficiency of large zooplankton	no dimension	0.7 ^S
β_{ZL}	Growth efficiency of large zooplankton	no dimension	0.3 ^S
Mor_{ZL0}	Large zooplankton mortality rate at 0 °C	$\text{m}^3 \text{mmolN}^{-1} \text{day}^{-1}$	0.022 ^S
K_{GraL}	Large zooplankton temperature coefficient for grazing	$^{\circ}\text{C}^{-1}$	0.0693 ^S
K_{MorZL}	Large zooplankton temperature coefficient for mortality	$^{\circ}\text{C}^{-1}$	0.0693 ^S
Predatory zooplankton			
GR_{maxPpl}	Predatory zooplankton maximum grazing rate on large phytoplankton at 0 °C	day^{-1}	0.1 ^S
GR_{maxPzs}	Predatory zooplankton maximum grazing rate on small zooplankton at 0 °C	day^{-1}	0.1 ^S
GR_{maxPzl}	Predatory zooplankton maximum grazing rate on large zooplankton at 0 °C	day^{-1}	0.3 ^S
λ_p	Ivlev constant of predatory zooplankton	$\text{m}^3 \text{mmolN}^{-1}$	1.4 ^S
<i>PL2ZP</i>	Predatory zooplankton threshold value for grazing on large phytoplankton	mmolN m^{-3}	0.040 ^S
<i>ZS2ZP</i>	Predatory zooplankton threshold value for grazing on small zooplankton	mmolN m^{-3}	0.040 ^S
<i>ZL2ZP</i>	Predatory zooplankton threshold value for grazing on large zooplankton	mmolN m^{-3}	0.040 ^S
α_{ZP}	Assimilation efficiency of predatory zooplankton	no dimension	0.7 ^S
β_{ZP}	Growth efficiency of predatory zooplankton	no dimension	0.3 ^S
Mor_{ZP0}	Predatory zooplankton mortality rate at 0 °C	$\text{m}^3 \text{mmolN}^{-1} \text{day}^{-1}$	0.12 ^S
K_{GraP}	Predatory zooplankton temperature coefficient for grazing	$^{\circ}\text{C}^{-1}$	0.0693 ^S

K_{MorZP}	Predatory zooplankton temperature coefficient for mortality	$^{\circ}\text{C}^{-1}$	0.0693 ^S
ψ_{PL}	Grazing inhibition coefficient of predatory zooplankton grazing on large phytoplankton	$\text{m}^3 \text{mmolN}^{-1}$	4.605 ^S
ψ_{ZS}	Grazing inhibition coefficient of predatory zooplankton grazing on small zooplankton	$\text{m}^3 \text{mmolN}^{-1}$	3.01 ^S
Light			
$AttSW$	Light attenuation due to seawater	m^{-1}	0.03 ^S
$AttPS$	Light attenuation due to small phytoplankton, self-shading coefficient	$\text{m}^2 \text{mmolN}^{-1}$	0.03 ^S
$AttPL$	Light attenuation due to large phytoplankton, self-shading coefficient	$\text{m}^2 \text{mmolN}^{-1}$	0.03 ^S
$frac$	Fraction of shortwave radiation that is photosynthetically active	no dimension	0.43 ^S
I_0	Threshold of light inhibition of nitrification	W m^{-2}	0.0095 ^{F06}
k_I	Light intensity at which light inhibition of nitrification is half-saturated	W m^{-2}	0.1 ^{F06}
Water column nitrification and aerobic decomposition			
Nit_0	Nitrification rate at 0 $^{\circ}\text{C}$	day^{-1}	0.003 ^S
$VP2N_0$	Decomposition rate at 0 $^{\circ}\text{C}$ (PON \rightarrow NH ₄)	day^{-1}	0.01 ^S
$VP2D_0$	Decomposition rate at 0 $^{\circ}\text{C}$ (PON \rightarrow DON)	day^{-1}	0.05 ^S
$VD2N_0$	Decomposition rate at 0 $^{\circ}\text{C}$ (DON \rightarrow NH ₄)	day^{-1}	0.02 ^S
$VO2S_0$	Decomposition rate at 0 $^{\circ}\text{C}$ (Opal \rightarrow Si(OH) ₄)	day^{-1}	0.01 ^S
K_{Nit}	Temperature coefficient for nitrification	$^{\circ}\text{C}^{-1}$	0.0693 ^S
K_{P2D}	Temperature coefficient for decomposition (PON \rightarrow DON)	$^{\circ}\text{C}^{-1}$	0.0693 ^S
K_{P2N}	Temperature coefficient for decomposition (PON \rightarrow NH ₄)	$^{\circ}\text{C}^{-1}$	0.0693 ^S
K_{D2N}	Temperature coefficient for decomposition (DON \rightarrow NH ₄)	$^{\circ}\text{C}^{-1}$	0.0693 ^S

K_{O_2S}	Temperature coefficient for decomposition (Opal→Si(OH) ₄)	°C ⁻¹	0.0693 ^S
Other parameters			
K_{Oxyg}	Oxygen concentration at which inhibition of nitrification and aerobic respiration are half-saturated	mmolO ₂ m ⁻³	3.0 ^{F13}
$Oxyg_{th}$	Oxygen concentration threshold below which no aerobic respiration or nitrification occurs	mmolO ₂ m ⁻³	6.0 ^{F13}
$RPO4N$	P: N ratio	mmolP mmolN ⁻¹	1/16 ^L
$RSiN$	Si: N ratio	mmolSi mmolN ⁻¹	1 ^S
$rOxNO_3$	Stoichiometric ratios corresponding to the oxygen produced per mol of nitrate assimilated during photosynthesis	mmolO ₂ mmolNO ₃ ⁻¹	138/16 ^{F13}
$rOxNH_4$	Stoichiometric ratios corresponding to the oxygen produced per mol of ammonium assimilated during photosynthesis	mmolO ₂ mmolNH ₄ ⁻¹	106/16 ^{F13}
$setVPON$	Sinking velocity of PON	m day ⁻¹	-5*
$setVOpal$	Sinking velocity of Opal	m day ⁻¹	-5*



796

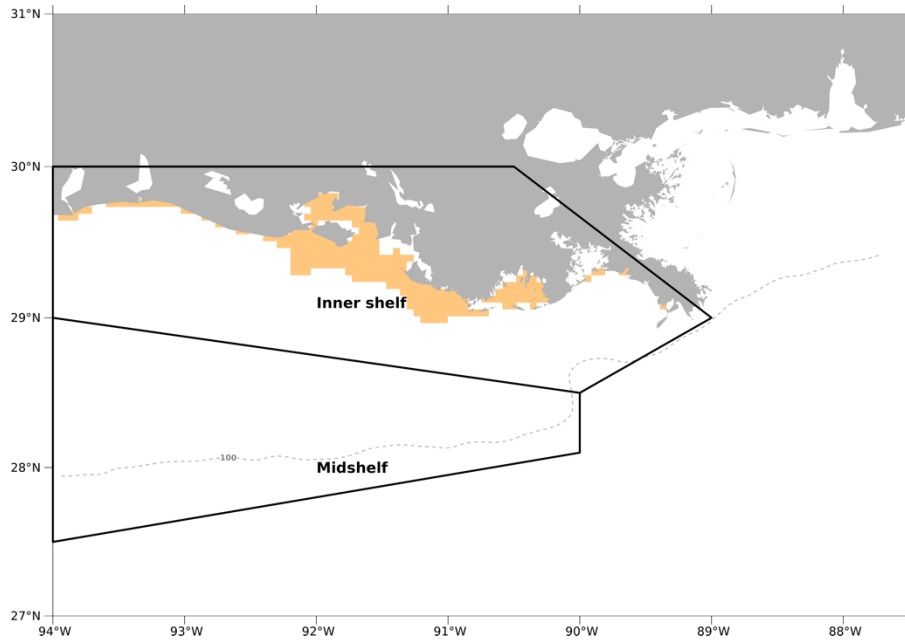
797 **Figure C1. Daily time series (2007–2020) of river discharges of freshwater, nitrate, phosphate, and silicate from the Mississippi and**
 798 **Atchafalaya Rivers.**

799 **Table C1. A correlation matrix of daily inorganic nutrient loads by the Mississippi River and the Atchafalaya River from 2007 to**
 800 **2020. Correlation coefficients shown are all significant ($p < 0.001$).**

	Mississippi nitrate+nitrite	Atchafalaya nitrate+nitrite	Mississippi phosphate	Atchafalaya phosphate	Mississippi silicate	Atchafalaya silicate
Mississippi nitrate+nitrite	1					
Atchafalaya nitrate+nitrite	0.9123	1				
Mississippi phosphate	0.8328	0.7577	1			
Atchafalaya phosphate	0.7517	0.7913	0.9155	1		
Mississippi silicate	0.8583	0.7795	0.8759	0.7942	1	

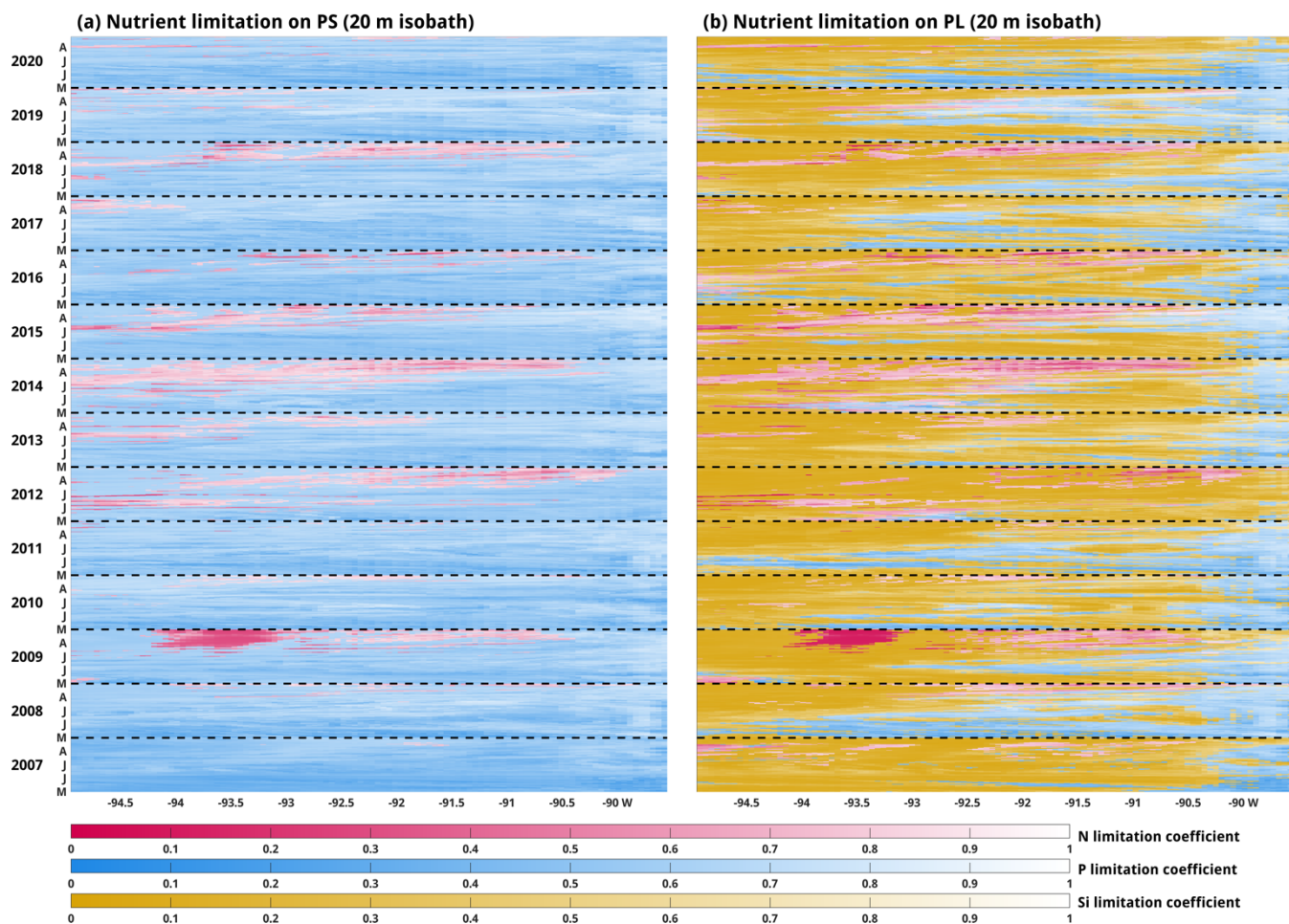
Atchafalaya silicate	0.7938	0.7956	0.8131	0.8148	0.9520	1
-------------------------	--------	--------	--------	--------	--------	---

801



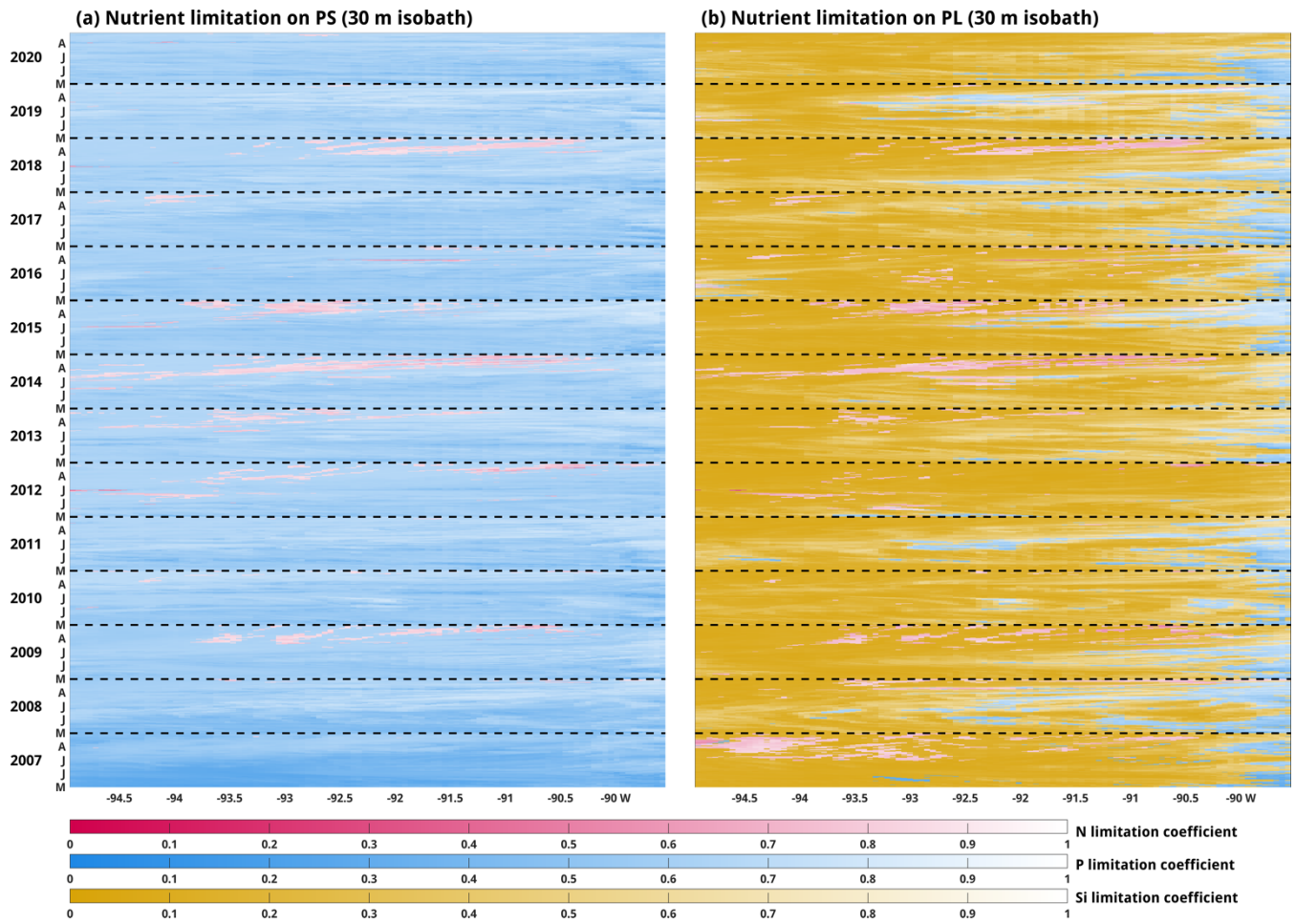
802

803 **Figure C2. The model computational meshes over which the regionally averaged diatom ratios were conducted for validation**
804 **purposes. The orange-patched region covers roughly the study regions in Schaeffer et al. (2012), while the regions restricted by two**
805 **black polygons are two regions (i.e., inner shelf and mid-shelf) where samples were collected in Chakraborty and Lohrenz's (2015)**
806 **study.**



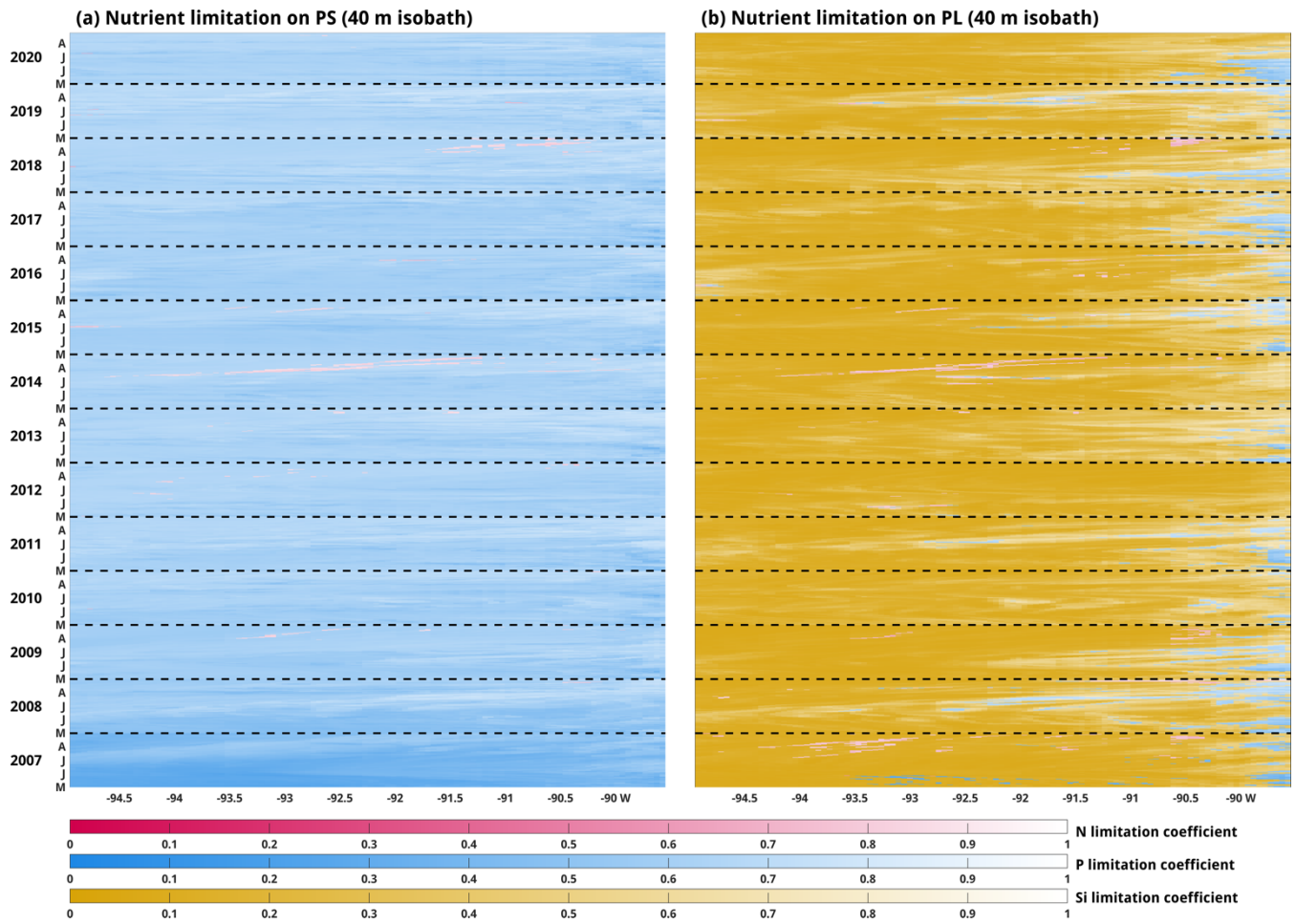
807

808 Figure C3. Evolution of depth-averaged nutrient limitation coefficients for (a) PS and (PL) along the 20 m isobath during late spring
 809 and summer. The notations of M, J, J, and A in the y-axis represent the first day of May, June, July, and August, respectively. Note
 810 that a lower (deeper colored) coefficient represents stronger limitations on phytoplankton growth. The dashed black lines indicate
 811 the time record on May 1 of each year.



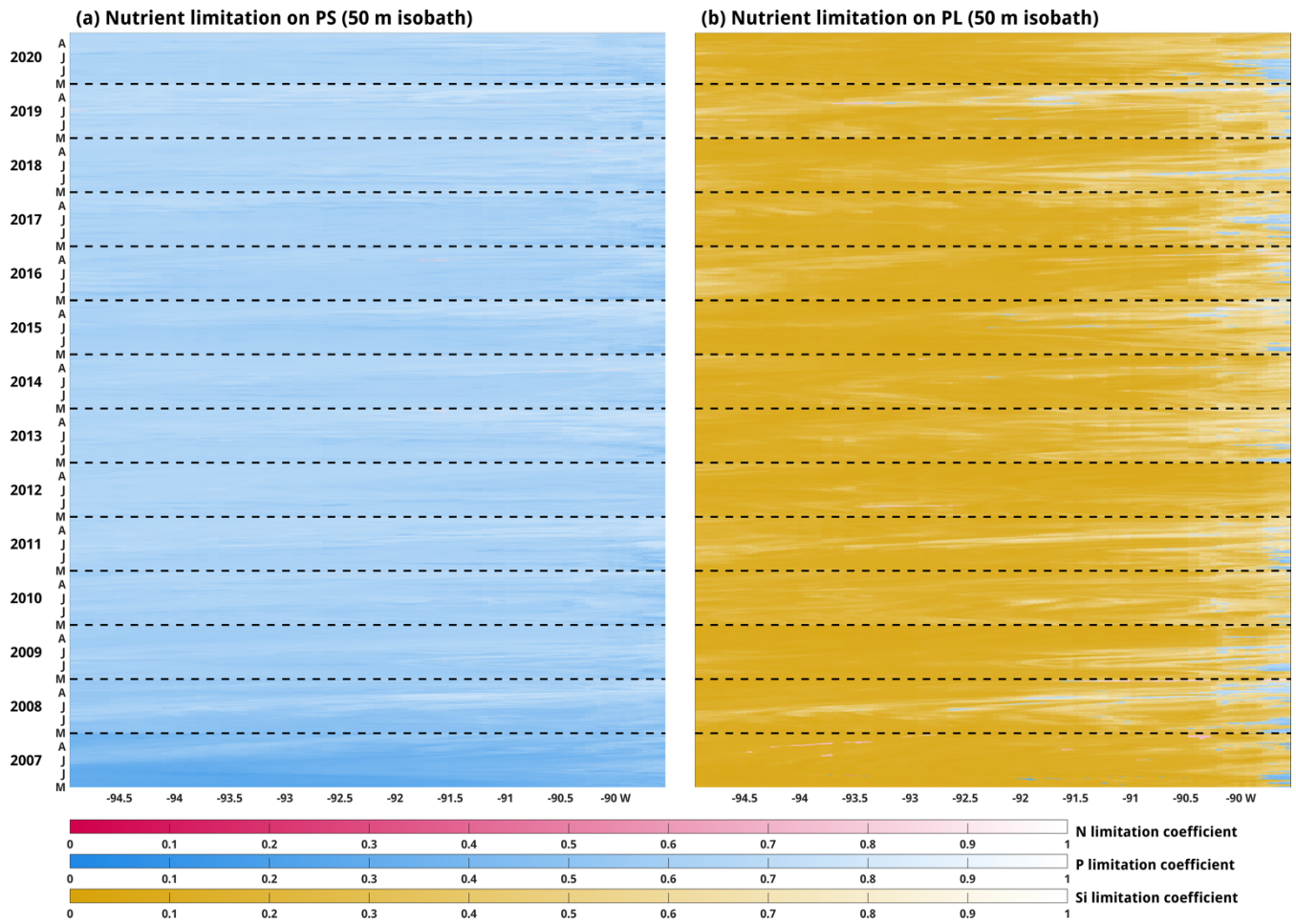
812

813 Figure C4. Same as Figure C3, but along the 30 m isobath.



814

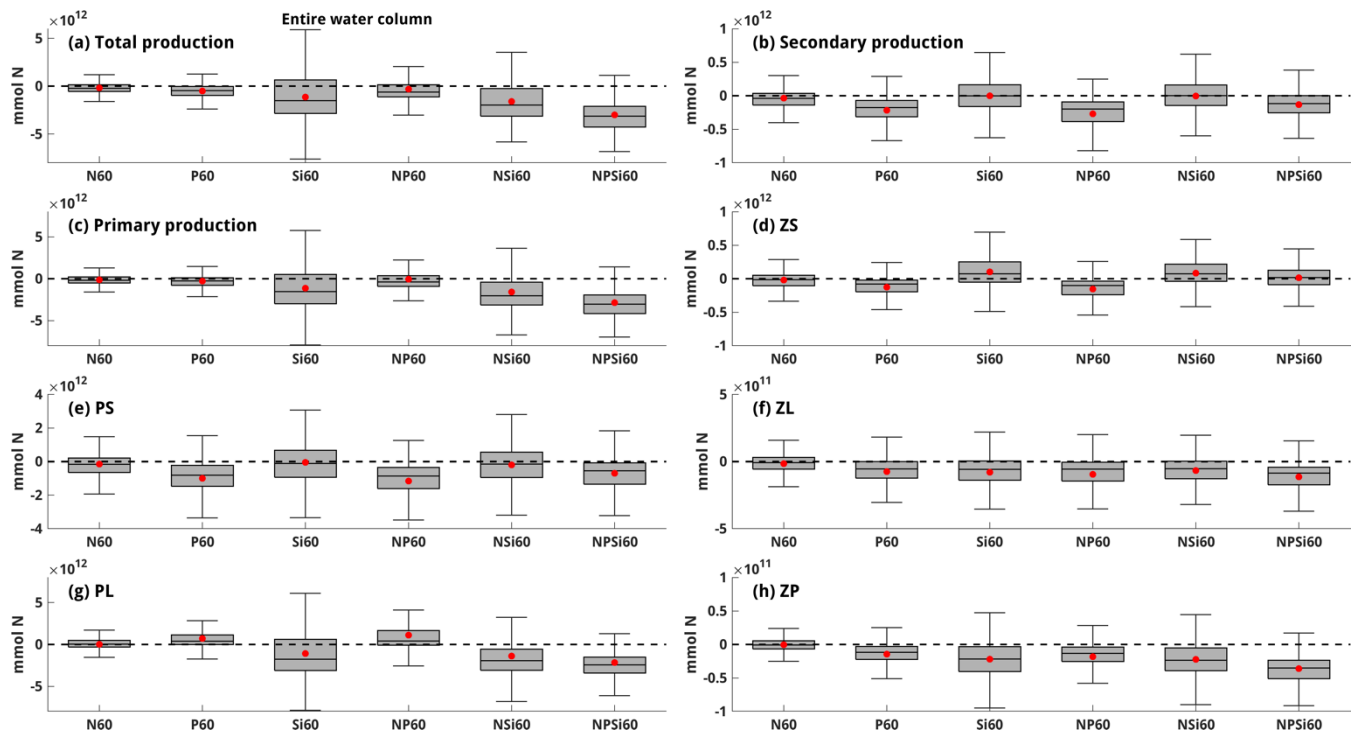
815 Figure C5. Same as Figure C3, but along the 40 m isobath.



816

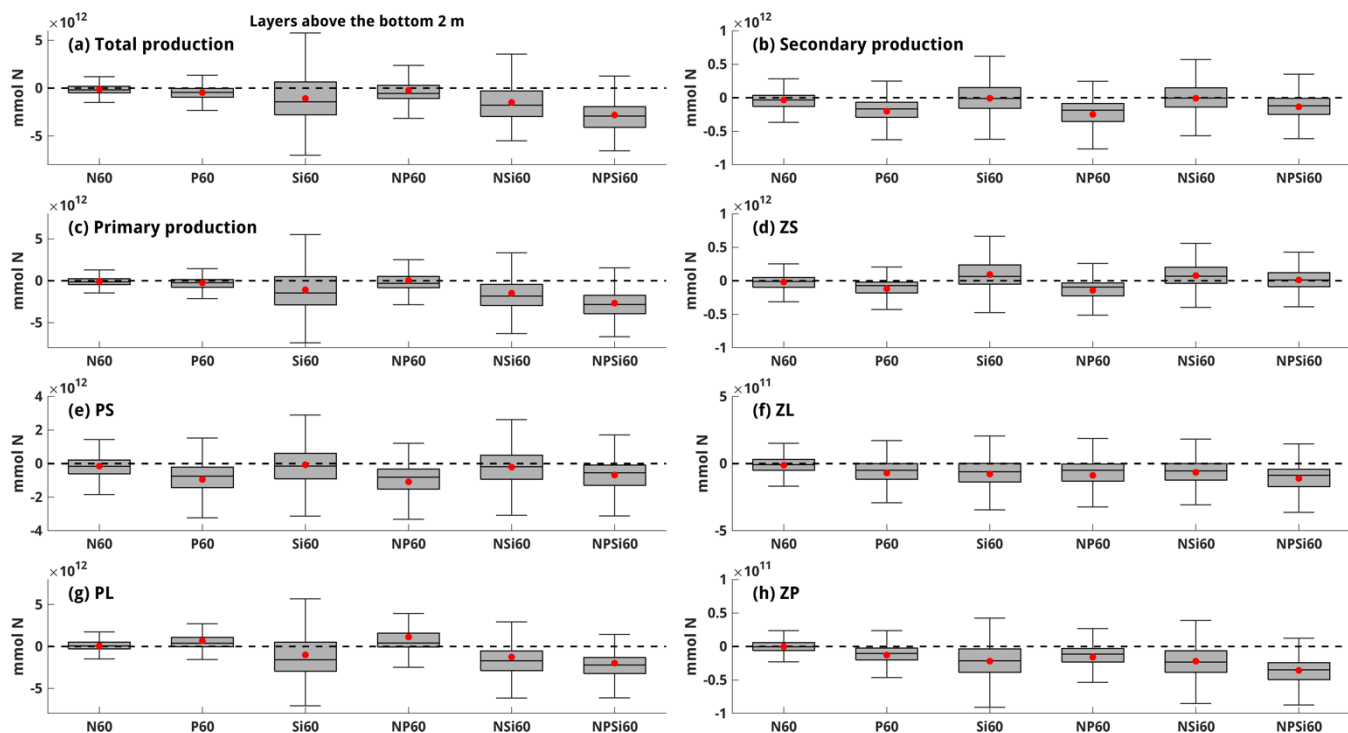
817 **Figure C6. Same as Figure C3, but along the 50 m isobath.**

818



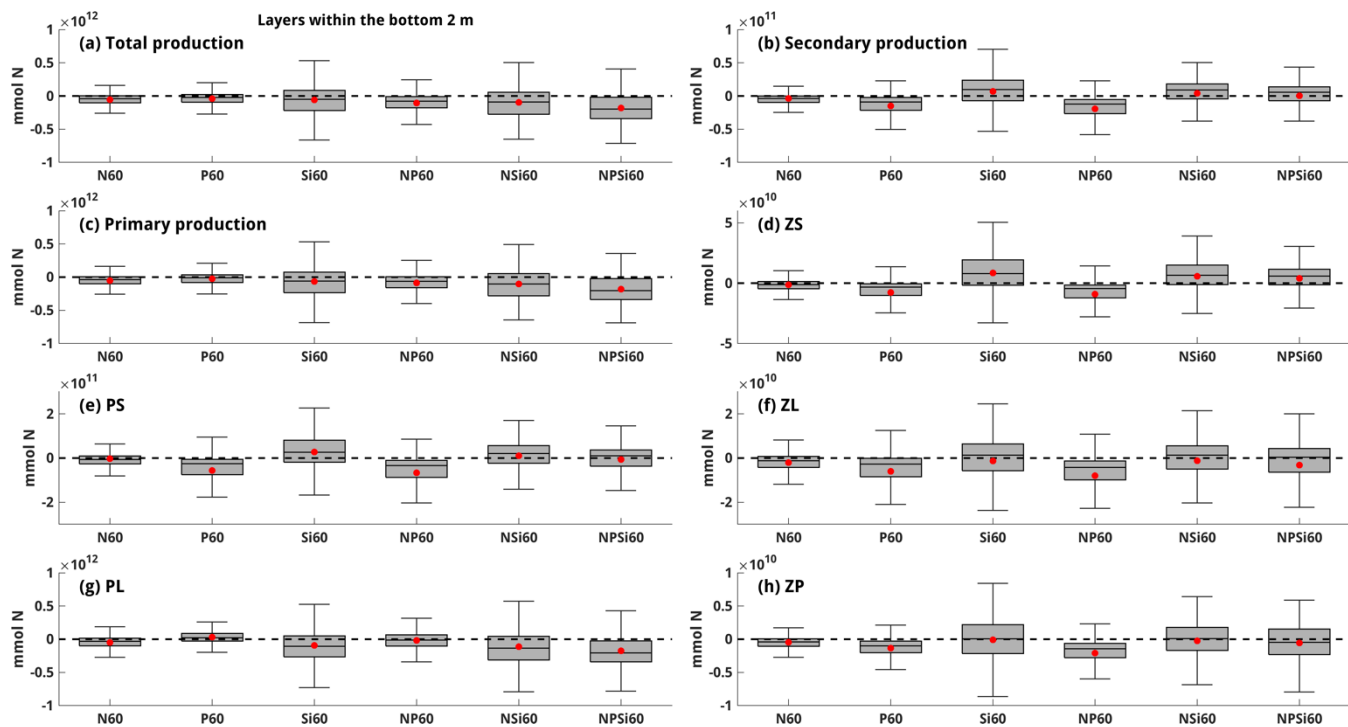
819

820 **Figure C7. Responses of (a) total production, (b) secondary production, (c) primary production, (d) ZS biomass, (e) PS biomass, (f)**
 821 **ZL biomass, (g) PL biomass, and (h) ZP biomass to the reductions in riverine nutrient loads. All biomass matrices were integrated**
 822 **over the entire water column and the LaTex shelf. Statistics shown are mean (red dots), median, first quartile, third quartile,**
 823 **minimum, and maximum derived from the differences between sensitivity tests and the control run during late spring and summer**
 824 **(May–August).**



825

826 **Figure C8.** Same as Fig. C7, but for integrated biomass over layers above the bottom 2 m.



827

828 **Figure C9.** Same as Fig. C7, but for integrated biomass at layers within 2 m above the bottom.

829 References

- 830 Del Amo, Y. and Brzezinski, M. A.: The chemical form of dissolved Si taken up by marine diatoms, *J. Phycol.*, 35, 1162–1170,
831 <https://doi.org/10.1046/j.1529-8817.1999.3561162.x>, 1999.
- 832 Anglès, S., Jordi, A., Henrichs, D. W., and Campbell, L.: Influence of coastal upwelling and river discharge on the phytoplankton community
833 composition in the northwestern Gulf of Mexico, *Prog. Oceanogr.*, 173, 26–36, <https://doi.org/10.1016/j.pocean.2019.02.001>, 2019.
- 834 Azam, F.: Silicic-acid uptake in diatoms studied with [⁶⁸Ge]germanic acid as tracer, *Planta*, 121, 205–212,
835 <https://doi.org/10.1007/BF00389321>, 1974.
- 836 Azam, F., Hemmingsen, B. B., and Volcani, B. E.: Role of silicon in diatom metabolism - V. silicic acid transport and metabolism in the
837 heterotrophic diatom *Nitzschia alba*, *Arch. Microbiol.*, 97, 103–114, <https://doi.org/10.1007/BF00403050>, 1974.
- 838 Bianchi, T. S., DiMarco, S. F., Cowan, J. H., Hetland, R. D., Chapman, P., Day, J. W., and Allison, M. A.: The science of hypoxia in the
839 northern Gulf of Mexico: A review, *Sci. Total Environ.*, 408, 1471–1484, <https://doi.org/10.1016/j.scitotenv.2009.11.047>, 2010.
- 840 Bleck, R.: An oceanic general circulation model framed in hybrid isopycnic-Cartesian coordinates, *Ocean Model.*, 4, 55–88,
841 [https://doi.org/10.1016/S1463-5003\(01\)00012-9](https://doi.org/10.1016/S1463-5003(01)00012-9), 2002.
- 842 Bleck, R. and Boudra, D. B.: Initial testing of a numerical ocean circulation model using a hybrid (quasi-isopycnic) vertical coordinate, *J.*
843 *Phys. Oceanogr.*, 11, 755–770, [https://doi.org/https://doi.org/10.1175/1520-0485\(1981\)011<0755:ITOANO>2.0.CO;2](https://doi.org/https://doi.org/10.1175/1520-0485(1981)011<0755:ITOANO>2.0.CO;2), 1981.
- 844 Boyer, T. P., Baranova, O. K., Coleman, C., Garcia, H. E., Grodsky, A., Locarnini, R. A., Mishonov, A. V., Paver, C. R., Reagan, J. R.,
845 Seidov, D., Smolyar, I. V., Weathers, K. W., and Zweng, M. M.: World Ocean Database 2018, Technical., edited by: Mishonov, A. V.,
846 NOAA Atlas NESDIS 87, 2018.
- 847 Chakraborty, S. and Lohrenz, S. E.: Phytoplankton community structure in the river-influenced continental margin of the northern Gulf of
848 Mexico, *Mar. Ecol. Prog. Ser.*, 521, 31–47, <https://doi.org/10.3354/meps11107>, 2015.
- 849 Chakraborty, S., Lohrenz, S. E., and Gundersen, K.: Photophysiological and light absorption properties of phytoplankton communities in
850 the river-dominated margin of the northern Gulf of Mexico, *J. Geophys. Res. Ocean.*, 122, 4922–4938,
851 <https://doi.org/10.1002/2016JC012092>, 2017.
- 852 Chapman, D. C.: Numerical treatment of cross-shelf open boundaries in a barotropic coastal ocean model., [https://doi.org/10.1175/1520-0485\(1985\)015<1060:ntocso>2.0.co;2](https://doi.org/10.1175/1520-0485(1985)015<1060:ntocso>2.0.co;2), 1985.
- 854 Cummings, J. A.: Operational multivariate ocean data assimilation, *Q. J. R. Meteorol. Soc.*, 131, 3583–3604,
855 <https://doi.org/10.1256/qj.05.105>, 2005.
- 856 Cummings, J. A. and Smedstad, O. M.: Variational Data Assimilation for the Global Ocean, in: *Data Assimilation for Atmospheric, Oceanic*
857 *and Hydrologic Applications*, vol. II, edited by: Park, S. K. and Xu, L., Springer Berlin Heidelberg, 303–343, https://doi.org/10.1007/978-3-642-35088-7_13, 2013.
- 859 Dortch, Q. and Whittedge, T. E.: Does nitrogen or silicon limit phytoplankton production in the Mississippi River plume and nearby regions?,
860 *Cont. Shelf Res.*, 12, 1293–1309, [https://doi.org/10.1016/0278-4343\(92\)90065-R](https://doi.org/10.1016/0278-4343(92)90065-R), 1992.
- 861 Feng, Y., Fennel, K., Jackson, G. A., DiMarco, S. F., and Hetland, R. D.: A model study of the response of hypoxia to upwelling-favorable
862 wind on the northern Gulf of Mexico shelf, *J. Mar. Syst.*, 131, 63–73, <https://doi.org/10.1016/j.jmarsys.2013.11.009>, 2014.
- 863 Fennel, K. and Laurent, A.: N and P as ultimate and proximate limiting nutrients in the northern Gulf of Mexico: Implications for hypoxia
864 reduction strategies, 15, 3121–3131, <https://doi.org/10.5194/bg-15-3121-2018>, 2018.
- 865 Fennel, K. and Testa, J. M.: Biogeochemical Controls on Coastal Hypoxia, *Ann. Rev. Mar. Sci.*, 11, 105–130,
866 <https://doi.org/10.1146/annurev-marine-010318-095138>, 2019.

- 867 Fennel, K., Wilkin, J., Levin, J., Moisan, J., O'Reilly, J., and Haidvogel, D.: Nitrogen cycling in the Middle Atlantic Bight: Results from a
868 three-dimensional model and implications for the North Atlantic nitrogen budget, *Global Biogeochem. Cycles*, 20, 1–14,
869 <https://doi.org/10.1029/2005GB002456>, 2006.
- 870 Fennel, K., Hetland, R., Feng, Y., and Dimarco, S.: A coupled physical-biological model of the Northern Gulf of Mexico shelf: Model
871 description, validation and analysis of phytoplankton variability, 8, 1881–1899, <https://doi.org/10.5194/bg-8-1881-2011>, 2011.
- 872 Fennel, K., Hu, J., Laurent, A., Marta-Almeida, M., and Hetland, R.: Sensitivity of hypoxia predictions for the northern Gulf of Mexico to
873 sediment oxygen consumption and model nesting, *J. Geophys. Res. Ocean.*, 118, 990–1002, <https://doi.org/10.1002/jgrc.20077>, 2013.
- 874 Fennel, K., Laurent, A., Hetland, R., Justic, D., Ko, D. S., Lehrter, J., Murrell, M., Wang, L., Yu, L., and Zhang, W.: Effects of model physics
875 on hypoxia simulations for the northern Gulf of Mexico: A model intercomparison, *J. Geophys. Res. Ocean.*, 121, 5731–5750,
876 <https://doi.org/10.1002/2015JC011516>, 2016.
- 877 Fiechter, J. and Moore, A. M.: Interannual spring bloom variability and Ekman pumping in the coastal Gulf of Alaska, *J. Geophys. Res.*
878 *Ocean.*, 114, 1–19, <https://doi.org/10.1029/2008JC005140>, 2009.
- 879 Flather, R. A.: A tidal model of the northwest European continental shelf, *Mem. la Soc. R. Sci. Liege*, 10, 141–164, 1976.
- 880 Fox, D. N., Teague, W. J., Barron, C. N., Carnes, M. R., and Lee, C. M.: The Modular Ocean Data Assimilation System (MODAS), *J.*
881 *Atmos. Ocean. Technol.*, 19, 240–252, [https://doi.org/10.1175/1520-0426\(2002\)019<0240:TMODAS>2.0.CO;2](https://doi.org/10.1175/1520-0426(2002)019<0240:TMODAS>2.0.CO;2), 2002.
- 882 Garcia, H. E., Weathers, K., Paver, C. R., Smolyar, I., Boyer, T. P., Locarnini, R. A., Zweng, M. M., Mishonov, A. V., Baranova, O. K.,
883 Seidov, D., and Reagan, J. R.: World Ocean Atlas 2018, Volume 3: Dissolved Oxygen, Apparent Oxygen Utilization, and Oxygen Saturation,
884 Technical., edited by: Mishonov, A. V., NOAA Atlas NESDIS 83, 38 pp., 2018.
- 885 Gomez, F. A., Lee, S. K., Liu, Y., Hernandez, F. J., Muller-Karger, F. E., and Lamkin, J. T.: Seasonal patterns in phytoplankton biomass
886 across the northern and deep Gulf of Mexico: A numerical model study, 15, 3561–3576, <https://doi.org/10.5194/bg-15-3561-2018>, 2018.
- 887 Große, F., Fennel, K., and Laurent, A.: Quantifying the Relative Importance of Riverine and Open-Ocean Nitrogen Sources for Hypoxia
888 Formation in the Northern Gulf of Mexico, *J. Geophys. Res. Ocean.*, 5451–5467, <https://doi.org/10.1029/2019jc015230>, 2019.
- 889 Haidvogel, D. B., Arango, H. G., Hedstrom, K., Beckmann, A., Malanotte-Rizzoli, P., and Shchepetkin, A. F.: Model evaluation experiments
890 in the North Atlantic Basin: Simulations in nonlinear terrain-following coordinates, *Dyn. Atmos. Ocean.*, 32, 239–281,
891 [https://doi.org/10.1016/S0377-0265\(00\)00049-X](https://doi.org/10.1016/S0377-0265(00)00049-X), 2000.
- 892 Helber, R. W., Townsend, T. L., Barron, C. N., Dastugue, J. M., and Carnes, M. R.: Validation Test Report for the Improved Synthetic
893 Ocean Profile (ISOP) System, Part I: Synthetic Profile Methods and Algorithm, 2013.
- 894 Hetland, R. D. and DiMarco, S. F.: How does the character of oxygen demand control the structure of hypoxia on the Texas-Louisiana
895 continental shelf?, *J. Mar. Syst.*, 70, 49–62, <https://doi.org/10.1016/j.jmarsys.2007.03.002>, 2008.
- 896 Justić, D. and Wang, L.: Assessing temporal and spatial variability of hypoxia over the inner Louisiana-upper Texas shelf: Application of
897 an unstructured-grid three-dimensional coupled hydrodynamic-water quality model, *Cont. Shelf Res.*, 72, 163–179,
898 <https://doi.org/10.1016/j.csr.2013.08.006>, 2014.
- 899 Justić, D., Rabalais, N. N., and Turner, R. E.: Simulated responses of the Gulf of Mexico hypoxia to variations in climate and anthropogenic
900 nutrient loading, *J. Mar. Syst.*, 42, 115–126, [https://doi.org/10.1016/S0924-7963\(03\)00070-8](https://doi.org/10.1016/S0924-7963(03)00070-8), 2003.
- 901 Justić, D., Bierman, V. J. J., Scavia, D., and Hetland, R. D.: Forecasting Gulf's Hypoxia: The Next 50 Years?, 30, 791–801, 2007.
- 902 Kishi, M. J., Kashiwai, M., Ware, D. M., Megrey, B. A., Eslinger, D. L., Werner, F. E., Noguchi-Aita, M., Azumaya, T., Fujii, M.,
903 Hashimoto, S., Huang, D., Iizumi, H., Ishida, Y., Kang, S., Kantakov, G. A., Kim, H. cheol, Komatsu, K., Navrotsky, V. V., Smith, S. L.,
904 Tadokoro, K., Tsuda, A., Yamamura, O., Yamanaka, Y., Yokouchi, K., Yoshie, N., Zhang, J., Zuenko, Y. I., and Zvalinsky, V. I.: NEMURO-
905 a lower trophic level model for the North Pacific marine ecosystem, *Ecol. Modell.*, 202, 12–25,
906 <https://doi.org/10.1016/j.ecolmodel.2006.08.021>, 2007.

- 907 Kristiansen, S. and Hoell, E. E.: The importance of silicon for marine production, *Hydrobiologia*, 484, 21–31,
908 <https://doi.org/10.1023/A:1021392618824>, 2002.
- 909 Laurent, A. and Fennel, K.: Simulated reduction of hypoxia in the northern Gulf of Mexico due to phosphorus limitation, *Elem. Sci. Anthr.*,
910 2, 1–12, <https://doi.org/10.12952/journal.elementa.000022>, 2014.
- 911 Laurent, A. and Fennel, K.: Time-Evolving, Spatially Explicit Forecasts of the Northern Gulf of Mexico Hypoxic Zone, *Environ. Sci.*
912 *Technol.*, 53, 14449–14458, <https://doi.org/10.1021/acs.est.9b05790>, 2019.
- 913 Laurent, A., Fennel, K., Hu, J., and Hetland, R.: Simulating the effects of phosphorus limitation in the Mississippi and Atchafalaya river
914 plumes, 9, 4707–4723, <https://doi.org/10.5194/bg-9-4707-2012>, 2012.
- 915 Laurent, A., Fennel, K., Wilson, R., Lehrter, J., and Devereux, R.: Parameterization of biogeochemical sediment-water fluxes using in situ
916 measurements and a diagenetic model, 13, 77–94, <https://doi.org/10.5194/bg-13-77-2016>, 2016.
- 917 Laurent, A., Fennel, K., Ko, D. S., and Lehrter, J.: Climate change projected to exacerbate impacts of coastal Eutrophication in the Northern
918 Gulf of Mexico, *J. Geophys. Res. Ocean.*, 123, 3408–3426, <https://doi.org/10.1002/2017JC013583>, 2018.
- 919 Li, Q. P., Franks, P. J. S., Landry, M. R., Goericke, R., and Taylor, A. G.: Modeling phytoplankton growth rates and chlorophyll to carbon
920 ratios in California coastal and pelagic ecosystems, *J. Geophys. Res. Biogeosciences*, 115, 1–12, <https://doi.org/10.1029/2009JG001111>,
921 2010.
- 922 Lohrenz, S. E., Fahnenstiel, G. L., Redalje, D. G., Lang, G. A., Dagg, M. J., Whitley, T. E., and Dortch, Q.: Nutrients, irradiance, and
923 mixing as factors regulating primary production in coastal waters impacted by the Mississippi River plume, *Cont. Shelf Res.*, 19, 1113–
924 1141, [https://doi.org/10.1016/S0278-4343\(99\)00012-6](https://doi.org/10.1016/S0278-4343(99)00012-6), 1999.
- 925 Marchesiello, P., McWilliams, J. C., and Shchepetkin, A.: Open boundary conditions for long-term integration of regional oceanic models,
926 *Ocean Model.*, 3, 1–20, [https://doi.org/10.1016/S1463-5003\(00\)00013-5](https://doi.org/10.1016/S1463-5003(00)00013-5), 2001.
- 927 Mattern, J. P., Fennel, K., and Dowd, M.: Sensitivity and uncertainty analysis of model hypoxia estimates for the Texas-Louisiana shelf, *J.*
928 *Geophys. Res. Ocean.*, 118, 1316–1332, <https://doi.org/10.1002/jgrc.20130>, 2013.
- 929 McCarthy, M. J., Carini, S. A., Liu, Z., Ostrom, N. E., and Gardner, W. S.: Oxygen consumption in the water column and sediments of the
930 northern Gulf of Mexico hypoxic zone, *Estuar. Coast. Shelf Sci.*, 123, 46–53, <https://doi.org/10.1016/j.ecss.2013.02.019>, 2013.
- 931 Milligan, A. J., Varela, D. E., Brzezinski, M. A., and Morel, F. M. M.: Dynamics of silicon metabolism and silicon isotopic discrimination
932 in a marine diatom as a function of pCO₂, *Limnol. Oceanogr.*, 49, 322–329, <https://doi.org/10.4319/lo.2004.49.2.0322>, 2004.
- 933 Mississippi River/Gulf of Mexico Watershed Nutrient Task Force: Action Plan for Reducing, Mitigating, and Controlling Hypoxia in the
934 Northern Gulf of Mexico, Washington, DC., 2001.
- 935 Mississippi River/Gulf of Mexico Watershed Nutrient Task Force: Gulf Hypoxia Action Plan 2008 for Reducing, Mitigating, and Controlling
936 Hypoxia in the Northern Gulf of Mexico and Improving Water Quality in the Mississippi River Basin, Washington, DC., 2008.
- 937 Moriarty, J. M., Harris, C. K., Friedrichs, M. A. M., Fennel, K., and Xu, K.: Impact of Seabed Resuspension on Oxygen and Nitrogen
938 Dynamics in the Northern Gulf of Mexico: A Numerical Modeling Study, *J. Geophys. Res. Ocean.*, 123, 7237–7263,
939 <https://doi.org/10.1029/2018JC013950>, 2018.
- 940 Murrell, M. C. and Lehrter, J. C.: Sediment and Lower Water Column Oxygen Consumption in the Seasonally Hypoxic Region of the
941 Louisiana Continental Shelf, 34, 912–924, <https://doi.org/10.1007/s12237-010-9351-9>, 2011.
- 942 Nelson, D. M. and Dortch, Q.: Silicic acid depletion and silicon limitation in the plume of the Mississippi River: Evidence from kinetic
943 studies in spring and summer, *Mar. Ecol. Prog. Ser.*, 136, 163–178, <https://doi.org/10.3354/meps136163>, 1996.
- 944 Nelson, D. M., Goering, John J., Kilham, S. S., and Guillard, R. R. L.: Kinetics of silicic acid uptake and rates of silica dissolution in the
945 marine diatom *Thalassiosira pseudonana*, *J. Phycol.*, 12, 246–252, <https://doi.org/https://doi.org/10.1111/j.1529-8817.1976.tb00510.x>, 1976.

- 946 Obenour, D. R., Michalak, A. M., and Scavia, D.: Assessing biophysical controls on Gulf of Mexico hypoxia through probabilistic modeling,
947 *Ecol. Appl.*, 25, 492–505, <https://doi.org/10.1890/13-2257.1>, 2015.
- 948 Olson, R. J.: Differential photoinhibition of marine nitrifying bacteria: a possible mechanism for the formation of the primary nitrite
949 maximum, *J. Mar. Res.*, 39, 227–238, 1981.
- 950 Parker, R. A.: Dynamic models for ammonium inhibition of nitrate uptake by phytoplankton, *Ecol. Modell.*, 66, 113–120,
951 [https://doi.org/10.1016/0304-3800\(93\)90042-Q](https://doi.org/10.1016/0304-3800(93)90042-Q), 1993.
- 952 Platt, T., Gallegos, C. L., and Harrison, W. G.: Photoinhibition of photosynthesis in natural assemblages of marine phytoplankton, *J. Mar.*
953 *Res.*, 38, 687–701, 1980.
- 954 Quigg, A., Sylvan, J. B., Gustafson, A. B., Fisher, T. R., Oliver, R. L., Tozzi, S., and Ammerman, J. W.: Going West: Nutrient Limitation
955 of Primary Production in the Northern Gulf of Mexico and the Importance of the Atchafalaya River, *Aquat. Geochemistry*, 17, 519–544,
956 <https://doi.org/10.1007/s10498-011-9134-3>, 2011.
- 957 Rabalais, N. N. and Baustian, M. M.: Historical Shifts in Benthic Infaunal Diversity in the Northern Gulf of Mexico since the Appearance
958 of Seasonally Severe Hypoxia, 12, <https://doi.org/10.3390/d12020049>, 2020.
- 959 Rabalais, N. N. and Turner, R. E.: Gulf of Mexico Hypoxia: Past, Present, and Future, *Limnol. Oceanogr. Bull.*, 28, 117–124,
960 <https://doi.org/10.1002/lob.10351>, 2019.
- 961 Rabalais, N. N., Turner, R. E., and Wiseman, W. J.: Gulf of Mexico hypoxia, a.k.a. “The dead zone,” *Annu. Rev. Ecol. Syst.*, 33, 235–263,
962 <https://doi.org/10.1146/annurev.ecolsys.33.010802.150513>, 2002.
- 963 Rabalais, N. N., Turner, R. E., Sen Gupta, B. K., Boesch, D. F., Chapman, P., and Murrell, M. C.: Hypoxia in the northern Gulf of Mexico:
964 Does the science support the plan to reduce, mitigate, and control hypoxia?, 30, 753–772, <https://doi.org/10.1007/BF02841332>, 2007a.
- 965 Rabalais, N. N., Turner, R. E., Gupta, B. K. S., Platon, E., and Parsons, M. L.: Sediments tell the history of eutrophication and hypoxia in
966 the northern Gulf of Mexico, *Ecol. Appl.*, 17, 129–143, <https://doi.org/10.1890/06-0644.1>, 2007b.
- 967 Robertson, R. and Hartlipp, P.: Surface wind mixing in the Regional Ocean Modeling System (ROMS), *Geosci. Lett.*, 4,
968 <https://doi.org/10.1186/s40562-017-0090-7>, 2017.
- 969 Rowe, G. T., Cruz Kaegi, M. E., Morse, J. W., Boland, G. S., and Escobar Briones, E. G.: Sediment community metabolism associated with
970 continental shelf hypoxia, northern Gulf of Mexico, 25, 1097–1106, <https://doi.org/10.1007/BF02692207>, 2002.
- 971 Saha, S., Moorthi, S., Pan, H.-L., Wu, X., Wang, J., Nadiga, S., Tripp, P., Kistler, R., Woollen, J., Behringer, D., Liu, H., Stokes, D.,
972 Grumbine, R., Gayno, G., Wang, J., Hou, Y.-T., Chuang, H.-Y., Juang, H.-M. H., Sela, J., Iredell, M., Treadon, R., Kleist, D., Van Delst,
973 P., Keyser, D., Derber, J., Ek, M., Meng, J., Wei, H., Yang, R., Lord, S., van den Dool, H., Kumar, A., Wang, W., Long, C., Chelliah, M.,
974 Xue, Y., Huang, B., Schemm, J.-K., Ebisuzaki, W., Lin, R., Xie, P., Chen, M., Zhou, S., Higgins, W., Zou, C.-Z., Liu, Q., Chen, Y., Han,
975 Y., Cucurull, L., Reynolds, R. W., Rutledge, G., and Goldberg, M.: NCEP Climate Forecast System Reanalysis (CFSR) 6-hourly Products,
976 January 1979 to December 2010, <https://doi.org/10.5065/D69K487J>, 2010.
- 977 Saha, S., Moorthi, S., Wu, X., Wang, J., Nadiga, S., Tripp, P., Behringer, D., Hou, Y.-T., Chuang, H., Iredell, M., Ek, M., Meng, J., Yang,
978 R., Mendez, M. P., van den Dool, H., Zhang, Q., Wang, W., Chen, M., and Becker, E.: NCEP Climate Forecast System Version 2 (CFSv2)
979 6-hourly Products, <https://doi.org/10.5065/D61C1TXF>, 2011.
- 980 Scavia, D., Evans, M. A., and Obenour, D. R.: A scenario and forecast model for gulf of mexico hypoxic area and volume, *Environ. Sci.*
981 *Technol.*, 47, 10423–10428, <https://doi.org/10.1021/es4025035>, 2013.
- 982 Schaeffer, B. A., Kurtz, J. C., and Hein, M. K.: Phytoplankton community composition in nearshore coastal waters of Louisiana, *Mar. Pollut.*
983 *Bull.*, 64, 1705–1712, <https://doi.org/10.1016/j.marpolbul.2012.03.017>, 2012.
- 984 Seitzinger, S. P. and Giblin, A. E.: Estimating denitrification in North Atlantic continental shelf sediments, in: Nitrogen Cycling in the North
985 Atlantic Ocean and its Watersheds, edited by: Howarth, R. W., Springer Dordrecht, 235–260, https://doi.org/10.1007/978-94-009-1776-7_7,
986 1996.

- 987 Shchepetkin, A. F. and McWilliams, J. C.: The regional oceanic modeling system (ROMS): A split-explicit, free-surface, topography-
988 following-coordinate oceanic model, *Ocean Model.*, 9, 347–404, <https://doi.org/10.1016/j.ocemod.2004.08.002>, 2005.
- 989 Shchepetkin, A. F. and McWilliams, J. C.: Correction and commentary for “Ocean forecasting in terrain-following coordinates: Formulation
990 and skill assessment of the regional ocean modeling system” by Haidvogel et al., *J. Comp. Phys.* 227, pp. 3595-3624, *J. Comput. Phys.*, 228,
991 8985–9000, <https://doi.org/10.1016/j.jcp.2009.09.002>, 2009.
- 992 Shropshire, T., Morey, S., Chassignet, E., Bozec, A., Coles, V., Landry, M., Swailethorp, R., Zapfe, G., and Stukel, M.: Quantifying
993 spatiotemporal variability in zooplankton dynamics in the Gulf of Mexico with a physical-biogeochemical model, 17, 3385–3407,
994 <https://doi.org/10.5194/bg-17-3385-2020>, 2020.
- 995 Sylvan, J. B., Quigg, A., Tozzi, S., and Ammerman, J. W.: Eutrophication-induced phosphorus limitation in the Mississippi River plume:
996 Evidence from fast repetition rate fluorometry, *Limnol. Oceanogr.*, 52, 2679–2685, <https://doi.org/10.4319/lo.2007.52.6.2679>, 2007.
- 997 Testa, J. M. and Michael Kemp, W.: Hypoxia-induced shifts in nitrogen and phosphorus cycling in Chesapeake Bay, *Limnol. Oceanogr.*,
998 57, 835–850, <https://doi.org/10.4319/lo.2012.57.3.0835>, 2012.
- 999 Thamatrakoln, K. and Hildebrand, M.: Silicon uptake in diatoms revisited: A model for saturable and nonsaturable uptake kinetics and the
1000 role of silicon transporters, *Plant Physiol.*, 146, 1397–1407, <https://doi.org/10.1104/pp.107.107094>, 2008.
- 1001 Turner, R. and Rabalais, N.: Nitrogen and phosphorus phytoplankton growth limitation in the northern Gulf of Mexico, *Aquat. Microb.*
1002 *Ecol.*, 68, 159–169, <https://doi.org/10.3354/ame01607>, 2013.
- 1003 Turner, R. E., Qureshi, N., Rabalais, N. N., Dortch, Q., Justić, D., Shaw, R. F., and Cope, J.: Fluctuating silicate:nitrate ratios and coastal
1004 plankton food webs, *Proc. Natl. Acad. Sci. U. S. A.*, 95, 13048–13051, <https://doi.org/10.1073/pnas.95.22.13048>, 1998.
- 1005 Turner, R. E., Rabalais, N. N., and Justić, D.: Predicting summer hypoxia in the northern Gulf of Mexico: Redux, *Mar. Pollut. Bull.*, 64,
1006 319–324, <https://doi.org/10.1016/j.marpolbul.2011.11.008>, 2012.
- 1007 Wang, L. and Justić, D.: A modeling study of the physical processes affecting the development of seasonal hypoxia over the inner Louisiana-
1008 Texas shelf: Circulation and stratification, *Cont. Shelf Res.*, 29, 1464–1476, <https://doi.org/10.1016/j.csr.2009.03.014>, 2009.
- 1009 Wanninkhof, R.: Relationship Between Wind Speed and Gas Exchange Over the Ocean, *J. Geophys. Res.*, 97, 7373–7382,
1010 <https://doi.org/10.1029/92JC00188>, 1992.
- 1011 Warner, J. C., Geyer, W. R., and Lerczak, J. A.: Numerical modeling of an estuary: A comprehensive skill assessment, *J. Geophys. Res. C*
1012 *Ocean.*, 110, 1–13, <https://doi.org/10.1029/2004JC002691>, 2005.
- 1013 Warner, J. C., Armstrong, B., He, R., and Zambon, J. B.: Development of a Coupled Ocean-Atmosphere-Wave-Sediment Transport
1014 (COAWST) Modeling System, *Ocean Model.*, 35, 230–244, <https://doi.org/10.1016/j.ocemod.2010.07.010>, 2010.
- 1015 Warner, J. C., Defne, Z., Haas, K., and Arango, H. G.: A wetting and drying scheme for ROMS, *Comput. Geosci.*, 58, 54–61,
1016 <https://doi.org/10.1016/j.cageo.2013.05.004>, 2013.
- 1017 Wawrik, B. and Paul, J. H.: Phytoplankton community structure and productivity along the axis of the Mississippi River plume in
1018 oligotrophic Gulf of Mexico waters, *Aquat. Microb. Ecol.*, 35, 185–196, <https://doi.org/10.3354/ame035185>, 2004.
- 1019 Yu, L., Fennel, K., and Laurent, A.: A modeling study of physical controls on hypoxia generation in the northern Gulf of Mexico, *J. Geophys.*
1020 *Res. Ocean.*, 120, 5019–5039, <https://doi.org/10.1002/2014JC010634>, 2015.
- 1021 Zang, Z., Xue, Z. G., Bao, S., Chen, Q., Walker, N. D., Haag, A. S., Ge, Q., and Yao, Z.: Numerical study of sediment dynamics during
1022 hurricane Gustav, *Ocean Model.*, 126, 29–42, <https://doi.org/10.1016/j.ocemod.2018.04.002>, 2018.
- 1023 Zang, Z., Xue, Z. G., Xu, K., Bentley, S. J., Chen, Q., D’Sa, E. J., and Ge, Q.: A Two Decadal (1993–2012) Numerical Assessment of
1024 Sediment Dynamics in the Northern Gulf of Mexico, 11, 938, <https://doi.org/10.3390/w11050938>, 2019.
- 1025 Zang, Z., Xue, Z. G., Xu, K., Ozdemir, C. E., Chen, Q., Bentley, S. J., and Sahin, C.: A Numerical Investigation of Wave-Supported Gravity

- 1026 Flow During Cold Fronts Over the Atchafalaya Shelf, *J. Geophys. Res. Ocean.*, 125, 1–24, <https://doi.org/10.1029/2019JC015269>, 2020.
- 1027 Zhao, Y. and Quigg, A.: Nutrient limitation in Northern Gulf of Mexico (NGOM): Phytoplankton communities and photosynthesis respond
1028 to nutrient pulse, *PLoS One*, 9, <https://doi.org/10.1371/journal.pone.0088732>, 2014.
- 1029
- 1030